

# **Neuromuscular Reflex Control for Prostheses and Exoskeletons**

Sandra Hnat

Bachelor of Science in Mechanical Engineering  
Cleveland State University  
May 2013

a candidacy proposal  
submitted in partial fulfillment of requirements for the degree  
DOCTOR OF ENGINEERING  
at the  
CLEVELAND STATE UNIVERSITY  
November 30, 2016

## **Committee Members**

Antonie J. van den Bogert  
Michael D. Hammonds  
Hanz Richter  
Jason Halloran  
Eric Schearer

# Contents

<b>1</b>	<b>Introduction, Motivation, and Research Objectives</b>	<b>1</b>
1.1	Background . . . . .	1
1.2	Specific Aims . . . . .	3
<b>2</b>	<b>Perturbation Experiments</b>	<b>6</b>
2.1	Experiment Design and Protocol . . . . .	6
2.2	Compensation of Inertial Artifacts . . . . .	7
2.3	Results . . . . .	10
2.4	Status and Contribution . . . . .	11
<b>3</b>	<b>Development of a Virtual Muscle Model</b>	<b>12</b>
3.1	Musculotendon Model . . . . .	12
3.2	Muscle Simulation and Evaluation . . . . .	14
3.3	Results . . . . .	16
3.3.1	Model Evaluation . . . . .	16
3.3.2	Speed and Accuracy . . . . .	17
3.4	Status and Contribution . . . . .	18
<b>4</b>	<b>Virtual Muscle Reflex (VMR) Control, Optimization, and Statistical Analysis</b>	<b>19</b>
4.1	Neuromuscular Reflex Controller . . . . .	19
4.2	Optimization . . . . .	20
4.3	Statistical Analysis . . . . .	23
4.4	Results . . . . .	23
4.4.1	Muscle Parameter Selection . . . . .	23
4.4.2	Ankle Joint Torque . . . . .	24
4.4.3	Statistical Analysis . . . . .	24
4.5	Status and Contribution . . . . .	27
<b>5</b>	<b>Hardware Implementation</b>	<b>29</b>
5.1	Ankle Virtual Muscles in the Indego Exoskeleton . . . . .	29
5.2	Hip and Knee VMR Control in Indego Exoskeleton . . . . .	30
5.3	Results . . . . .	31
5.4	Status and Contribution . . . . .	32

<b>6</b>	<b>Timeline for Remaining Research Objectives</b>	<b>34</b>
<b>A</b>	<b>Motion Capture Marker Set</b>	<b>35</b>
<b>B</b>	<b>Musculotendon Model</b>	<b>37</b>
<b>C</b>	<b>First-order Rosenbrock Solver for Muscle Dynamics</b>	<b>40</b>
<b>D</b>	<b>Reflex Model</b>	<b>42</b>
D.1	Ankle Reflexes . . . . .	42
D.2	Knee and Hip Reflexes . . . . .	43

# List of Tables

2.1	Root-mean-square (RMS) of the pitch moment before and after compensation. Compensation was performed by subtracting the predicted pitch moment from the measured value. . . . .	10
4.1	The mean and standard deviation of the RMS difference between the experimental and predicted torques, using several different muscle parameters in the optimization . . . . .	24
B.1	Muscle parameters used in the three-element Hill-model which describe muscle contraction and activation dynamics . . . . .	39

# List of Figures

2.1	MATLAB Simulink diagram for creating random belt velocities, in which a random acceleration signal is generated with Gaussian white noise. Belt velocity is obtained by integrating the signal and filtering with a high-pass Butterworth filter to reduce integration drift . . . . .	7
2.2	The treadmill with coordinate system, cameras (circled in orange), projection screen, and safety rope. . . . .	8
2.3	A diagram of the treadmill with coordinate system, where the red arrows describe the rotation of the treadmill roller which will introduce errors in pitch moment in measured ground reaction forces ( $M_x$ , in this system) . . .	9
2.4	Measured (black dotted) and predicted (red) pitch moment for the slow (top) and fast (bottom) speeds, with $R^2$ values of 72.08% and 96.75%, respectively. Only a small section of the 6-minute trial is shown. . . . .	10
3.1	Standard force-length (left) and force-velocity (right) of the contactile element (CE) in Hill-type muscle models, where negative and positive velocities represent shortening and lengthening, respectively . . . . .	13
3.2	Typical three-element Hill-type muscle model, consisting of a contractile element ( $CE$ ), parallel and series elastic elements ( $PEE$ , $SEE$ ), pennation angle ( $\phi$ ) and viscous damping in parallel to the $CE$ . . . . .	14
3.3	Overview of the Virtual Muscle Reflex (VMR) controller, where the inputs to the model are the muscle length $L_m$ and neural excitation signal $u$ , and the output is the muscle force which can be multiplied by the moment arm to obtain the joint torque . . . . .	15
3.4	Step-input signal for the muscle model validation (left) and sinusoidal input signals with 1 Hz frequency (right) for evaluating the speed and accuracy of the model . . . . .	16
3.5	Predicted muscle forces (top) and torques (bottom) with constant joint angles $q(t)$ held at $0^\circ$ and step-control signal $u$ randomly applied throughout the simulation. . . . .	17
3.6	Accuracy is effected by the integrator step size (left) and computation speed (right). Error was quantified as a percentage of the maximum moments in the knee and ankle. Real-time is indicated by the dashed red line, which is faster than 30 seconds. These results indicate that torques can be obtained in a simulation of muscle dynamics with accurate results and minimal computation time. . . . .	18

3.7	Accuracy vs. step size (left) and computation speed (right) using the VMR system in the C-programming language. All step sizes achieved real-time results, including an extremely small step size of 0.001 ms . . . . .	18
4.1	The parameters of the VMR system can be determined by minimizing the difference between the torque obtained through the experiment and inverse dynamics, $\tau_{exp}$ , and the torque produced by the neuromuscular reflex model $\tau_{VMR}$ . . . . .	21
4.2	The change in objective function as a function of the number of iterations of the optimization algorithm. In this example, the number of generations should be lowered to reduce the computation expense of the optimization . .	22
4.3	Measured (black) and predicted (red dashed) joint torque, zoomed to only a few seconds of the 8 minute walking trial, for clarity. Note that negative torque corresponds to ankle plantarflexion . . . . .	25
4.4	Measured (blue) and predicted (red) joint torque as a function of the gait cycle	25
4.5	Correlation between measured and predicted joint ankle torque at 60% of the gait cycle. Note that each point represents one data point for every gait cycle, in this case $N = 470$ gait cycles . . . . .	26
4.6	Coefficient of determination $R^2$ as a function of time in the gait cycle. Each correlation coefficient was based on 470 gait cycles in this 8-minute recording	27
5.1	Ankle joint torque (top) of the isometric simulation tests with the plantarflexor (PF) muscles fully activated (left) and dorsiflexor (DF) muscles fully activated (right) . . . . .	31
5.2	Ankle joint torque (top) of the isokinetic simulation tests with the PF muscles fully activated (left) and the DF muscles fully activated (right) when the ankle angle was moved in a sawtooth trajectory (bottom) . . . . .	32
5.3	Indego Exoskeleton on a Biodex rehabilitation machine at the Cleveland Clinic. The Indego is programmed with virtual muscles of the Soleus, Tibialis Anterior, and Gastrocnemius, where the knee joint behaves as though it were an ankle . . . . .	33
6.1	Projected timeline for completing outstanding research objectives . . . . .	34
A.1	Full-body marker set consisting of 47 markers used in the perturbation experiments . . . . .	35
A.2	Detailed locations of the 47 markers used in the marker set . . . . .	36

## **Abstract**

We hypothesize that a more muscle-like actuation system, including spinal reflexes, is capable of replicating able-bodied locomotion in powered prosthetic devices or exoskeletons. We will invent a new controller that combines virtual muscles and spinal reflexes, in which control parameters are identified through optimizations using human experimental data of perturbed walking. Statistical analyses will verify the effectiveness of the control in describing the variations within and between gait cycles, as well as predict the capability of reflex controls in responding to external perturbations. The new controller will be implemented in hardware, in which joint torque produced by the electric motors should mimic the standard torque trajectories observed in our able-bodied experiments. Preliminary results verify that: (1) an implicit formulation of muscle dynamics can produce real-time simulation of muscle dynamics with excellent accuracy and (2) a reflex controller of the ankle can sufficiently reproduce the joint torque profiles exhibited by test subjects in perturbation experiments.

# Chapter 1

## Introduction, Motivation, and Research Objectives

### 1.1 Background

The human brain can be described as a highly accurate and rapidly functioning super-computer. Complex networks of approximately 100 billion neurons regulate every aspect of human cognition, perception, and movement [1, 2]. Though the brain's operation is nearly perfect, studying its processes is essential for developing assistive devices which restore functionality to individuals with physical limitations or impaired sensory feedback. Recent prosthetic devices and wearable exoskeletons improve the quality of life for persons with an amputation or spinal cord injury. The increasing prevalence of cardiovascular disease and diabetes [3], coupled with physical trauma from work-related accidents or wars [4], facilitate the demand for advancing the performance of available assistive devices.

Recently, the design of modern prostheses and exoskeletons focuses on developing sophisticated controllers capable of closely replicating able-bodied gait. Active prosthetic and exoskeleton devices are equipped with torque-driven electric motors at the joints, which can be controlled to produce typical joint torque curves observed in human locomotion [5]. Though various control strategies for active, lower-limb prostheses have been proposed, including time-varying impedance controllers [6, 7], able-bodied walking is not usually achieved. Similarly, wearable exoskeletons are capable of restoring mobility to persons with lower-limb paralysis. However, the phase-based, proportional-derivative (PD) controllers typically used in exoskeletons produce stagnated, unnatural gait [8].

In the human body, neurological input signals sent from the brain activate motor neurons which produce muscle contractions. Since the muscle is rigidly attached to the bone, the shortening or lengthening of muscle groups causes rotation of the joints, resulting in movement. A more muscle-like actuation system, including the biarticular nature and nonlinear elastic properties of muscles, may simply feedback control and improve performance and stability while achieving natural gait mechanics [9].

Rather than build muscle-like hardware, a real-time simulation of muscle dynamics can control the torque generated by electric motors. However, the underlying controller which produces the neural excitations that activate muscles is challenging to model. The various



strategies used by the brain to control human motion is not yet readily understood and these complex models would be incapable of solving quickly enough for real-time applications in modern hardware. More simplified, neurologically-inspired controllers have recently emerged as a viable method of obtaining stable gait while considering the human actuation system [10, 11].

Several mathematical models attempt to describe the firing of action potentials across motor neurons which synapse on skeletal muscles to generate ambulation. The most common artificial neuron model is the Hodgkin-Huxley model [12], in which total membrane current is calculated through a set of four differential equations describing the probability of an open voltage-gated channel along the neuron membrane. Such neuron models have been evaluated through experimentation using giant axons in squids. However, the complex locomotion of animals and quadruped humans requires millions of neurons. Modeling this complicated, extensive network becomes impractical and computationally demanding, thereby preventing its usage in real-time applications.

However, legged locomotion in animals can be described by central pattern generators (CPG), or neural networks in the spinal cord which produce the cyclical rhythms of locomotion without requiring sensory feedback from the peripheral nervous system [13, 14]. CPGs modulate spinal reflexes in order to produce locomotion without requiring input from the cerebral cortices. Generally, these neuron models are limited to a single pair of flexor and extensor muscles, known as coupled neural oscillators. Matsuoka’s neural oscillator produces a rhythmic generation of neural signals using pairs of mutually inhibiting neurons [15]. Adaptive neurons change their firing rates in response to the frequency of sensory stimuli [1]. Modified models include sensory feedback for coupling to bipedal, mechanical systems [16].

Since neural action potentials are defined by a prescribed amplitude and frequency, neural oscillators may be designed without biological-inspiration, such as Hopf’s oscillator [17]. Self-synchronizing neural signals that produce bipedal locomotion can also be obtained through nonlinear control theory [18]. Though Hopf’s oscillator and other CPG controllers can produce a stable limit cycle, their usage is generally limited to simpler controllers in quadruped robots [10, 11] or anguilloform robots [19]. This is because the fundamental basis of CPGs has not been identified in bipedal locomotion and the architecture of these models vary significantly.

Spinal reflex models are an appealing alternative to both the unknown architecture of CPG controllers and the computational expense of neuron models. In spinal reflexes, complex neural inputs from the brain are bypassed by directly driving the activation of muscle dynamics using sensory feedback information from the leg. This combination of an autonomous, neuromuscular reflex controller has been shown to produce stable walking in both simulation and hardware [20, 21, 22]. Proportional-derivative (PD) control is required to maintain postural stability of the trunk. PD control can be loosely correlated to human control strategies, as neurological tracts in the spinal cord carry sensory input to the cerebellum to correct for errors [2].

It has been shown that reflex controllers can more readily adapt to environmental disturbances than the typical impedance controllers used in many active prosthetic devices [23]. Though impedance controllers can successfully generate realistic joint torques, these controllers are sensitive to environmental disturbances and require additional control strategies

in the event of a trip or fall [24, 25]. Since reflex models solely rely on muscle force feedback, any disturbance in the environment (sloped terrain or external perturbations) will be sensed by reflexes due to the reactive change in muscle forces [22]. Therefore, developing distinct controllers to handle a wide range of situations is not required.

Though Geyer and Herr’s reflex controller [20] produces natural gait in simulated environments [20], many properties of the muscle models are computationally expensive and not included in hardware, thereby removing the stabilizing advantages of muscle dynamics. A real-time Virtual Muscle Reflex (VMR) system with an implicit formulation of muscle dynamics [26] will allow for these properties of muscles to be fully realized in real-time microcontrollers.

Additionally, these reflex models have not been tuned or validated using human walking data obtained through experiments. Here, we investigate the possibility of using a VMR system in order to determine if muscle reflexes are not only capable of reproducing able-bodied walking, but can also sufficiently replicate the variations in human joint moments within and between gait cycles when subjected to random mechanical perturbations. By forcing the human to recover from external perturbations, their respective reactive actions can be used to define the nature of the reflex controller.

## 1.2 Specific Aims

To address these open research questions, the long-term goal of this proposal is to introduce a novel VMR system for prosthetic devices. We hypothesize that a more biologically-inspired controller may be able to achieve able-bodied locomotion through a combination of virtual muscles and spinal reflexes based on data collected from human subjects under the effect of external perturbations. The VMR system will be experimentally validated in both simulation and hardware.

The study has the following research objectives:

1. **Perturbation Experiments.** Perturbation experiments will provide a rich enough data set to identify the fundamental aspects of human control, particularly in spinal reflexes. Test subjects will walk on an instrumented treadmill capable of producing random perturbations by varying the belt speed. A combination of motion capture and force plates will measure the movement and ground reaction forces (GRFs) of the test subject. Using standard inverse dynamics techniques, the joint angles and joint torques can be estimated using the motion capture and force plate data.

**Status:** Completed.

**Contribution:** A novel method to correct GRF measurements for inertial artifacts.

2. **Development of a Virtual Muscle Model.** A muscle model of the lower limb will produce the joint torque which actuate the electric motors of a prosthetic device or exoskeleton. Inputs to the muscle model are the joint angles,  $q(t)$ , which define the muscle length,  $L_m$ . During the development phase, these joint angles will be provided from the human perturbation experiments. However, in hardware, these joint angles will be obtained through encoders of the prosthesis or exoskeleton. Before its implementation in hardware, the muscle model must be evaluated in simulation to

determine its ability to produce accurate results while reducing the computation time.  
**Status:** Completed.

**Contribution:** A new method to accurately simulate muscle dynamics in real-time.

3. **Incorporation of Neuromuscular Reflexes.** Another input to the muscle model are the neural excitation signals,  $u(t)$ , which govern the muscle activations. The autonomous, positive force feedback reflex model of Geyer and Herr [20] will exclusively be used in the VMR system. Initially, the reflex controller will be considered for the ankle only, as the equations of ankle reflexes are simple and only marginally influenced by the movements of the hip and knee. However, a convenient platform for hardware implementation is the Indego Exoskeleton (Parker Hannifin Corporation, Mayfield Heights, Ohio, USA), equipped with electric motors at the hip and knee. After the VMR system demonstrates its ability to mimic ankle torque in simulation, the reflex model will be expanded to include the other two joints in the leg.

**Status:** Ankle reflexes have been tested in simulation. Next steps include extending the controller to the hip and knee.

**Contribution:** A method of combining reflex controllers and a muscle model representing the stabilizing properties of muscle dynamics, in real-time.

4. **Optimization of VMR Control Parameters.** Optimization techniques will be used to obtain the best possible reflex controller for describing the joint torques exhibited by test subjects. By minimizing the difference between the measured torque from the experiment and the predicted torque from the VMR model, the parameters of the reflex controller can be identified. A statistical analysis of the VMR system performance will provide insight to its capabilities. Statistical information of interest include: (1) the correlation of the data to a fitted regression line ( $R^2$ ) as a function of the gait cycle, (2) the relationship between the measured and predicted torque throughout each point in the gait cycle, and (3) a cross-validation of results within and between test subjects and treadmill speeds.

**Status:** Optimization methods were successful in identifying the parameters for the ankle reflexes. A partial statistical analysis has been performed on ankle control.

**Contribution:** (1) A VMR system can predict both human walking and reactive control based on perturbation experiments and (2) a statistical method to realize the full capabilities of neuromuscular reflex control.

5. **Hardware Implementation.** The VMR system will be programmed in the Indego by modifying the preexisting, phase-based, proportional-derivative controller [8] in MATLAB Simulink (Mathworks, Natick, Massachusetts, USA). The hardware test is separated into two distinct phases. Initially, the Indego will be programmed with ankle muscle control without reflexes in order to observe the passive properties of the virtual muscle. Using a Biodex rehabilitation system (Biodex Medical Systems, Shirley, New York, USA), the Indego will perform the standardized isokinetic and isometric tests used for rehabilitation [27, 28, 29]. Secondly, the ankle controller in the Indego will be replaced with the appropriate hip and knee muscles and reflexes. This will be used as a demonstration project of the reflex controller in an exoskeleton.

**Status:** Ankle muscles have been added in the Indego and verified through visual

observation. Future steps include testing on the Biodex, adding the remaining muscle groups of the lower leg, and programming the reflexes of all joints.

***Contribution:*** Neuromuscular reflex controllers have never been implemented in an exoskeleton, nor in a device with an actuated hip.

The remainder of the proposal is organized as follows. The development of the perturbation experiments are detailed in Chapter 2, while the modeling and validation of the muscle model is described in Chapter 3. A description of the reflex controller, including optimization methods and statistical analyses, are discussed in Chapter 4. Lastly, a hardware implementation plan for programming the VMR system in the Indego exoskeleton is described in Chapter 5. Each of these chapters includes both the methodology and the results of any completed work, as well as a section summarizing the current status of the research and its contribution to the scientific field. An implementation plan for completing the remaining objectives is briefly outlined in Chapter 6.

# Chapter 2

## Perturbation Experiments

A modern gait lab is able to collect a variety of kinematic, kinetic, and physiological data from humans during gait, which can be used to drive the design of a more human-like controller. The responses of humans when subjected to external perturbations can estimate the features of the human control system. In this section, we describe the design study for perturbing test subjects during walking.

The experimental protocol is outlined in Section 2.1, including a brief description of calculating joint torques and angles through inverse dynamics. Additionally, a method for compensating inertial artifacts induced by the movement of the treadmill is detailed in Section 2.2, in which the results are shown in Section 2.3.

### 2.1 Experiment Design and Protocol

Walking data from 15 participants, including 4 females and 11 males, with an average age of  $24 \pm 4$  years, height of  $1.75 \pm 0.09$  m, and mass of  $74 \pm 13$  kg was used in the study [30]. The study was approved by the Institutional Review Board of Cleveland State University (29904-VAN-HS) and all subjects were required to provide written informed consent. Test subjects walked for 8 minutes on an instrumented treadmill at 3 perturbed speeds (0.8, 1.2, and 1.6 m/s), with 1 minute of unperturbed walking at the start and end of the trial. Subjects were perturbed using random belt acceleration signals generated in MATLAB Simulink, as shown in Figure 2.1.

To create the perturbation signals, we started by generating random acceleration signals, sampled at 100 Hz, using the discrete-time Gaussian white noise block followed by a saturation block set at the maximum belt acceleration of  $15 \text{ m/s}^2$ . The signal was then integrated to obtain belt speed and high-pass filtered with a second-order Butterworth filter to eliminate drift. One of the three mean speeds were then added to the signal and limited between 0 m/s and 3.6 m/s. The cutoff frequencies of the high-pass filter, as well as the variance in the acceleration signal, were manually adjusted until acceptable standard deviations for each mean speed were obtained: 0.06 m/s, 0.12 m/s and 0.21 m/s for the 3 speeds, respectively. This ensured that the test subjects were sufficiently perturbed at  $\pm 10\%$  of each speed while remaining within the limits of our equipment.

The experimental protocol consisted of both static measurements (see Section 2.2) and

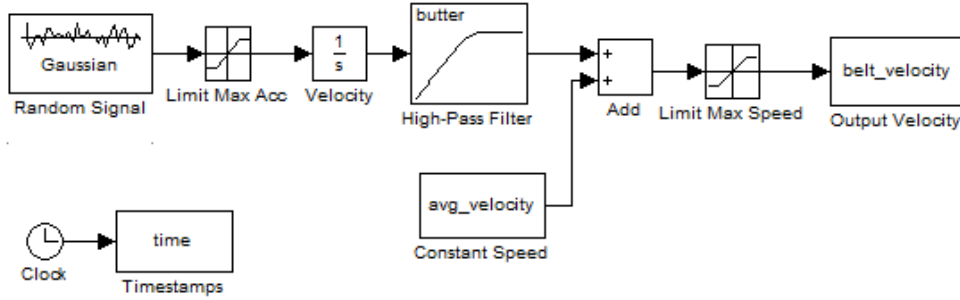


Figure 2.1: MATLAB Simulink diagram for creating random belt velocities, in which a random acceleration signal is generated with Gaussian white noise. Belt velocity is obtained by integrating the signal and filtering with a high-pass Butterworth filter to reduce integration drift

walking on the treadmill for 10 minutes under both unperturbed and perturbed conditions. All trials were performed on the same day, with the option of breaks between trials. Subjects changed into athletic shoes, shorts, a sports bra, a baseball cap, and a rock climbing harness. Then, a full-body, standard 47-marker set was applied directly to the skin. Details of the marker set can be referenced in Appendix A.

The data was collected in the Parker Hannifin Laboratory for Human Motion and Control at Cleveland State University. Experiments were performed on a 6 degree-of-freedom (DOF), split-belt instrumented treadmill, with lateral translation and pitch rotation capabilities (VG005-A, Motekforce Link, Amsterdam, Netherlands). The belt speed signals generated from Simulink were used to control the belt speed through software (D-Flow 3.16.2, Motekforce Link) which also recorded GRFs at a 100 Hz sampling rate. A 10 Osprey camera motion capture system paired with the Cortex 3.1.1.1290 software (Motion Analysis, Santa Rosa, CA, USA) measured the kinematics of the test subjects. Figure 2.2 shows the layout of the equipment and the coordinate system used by the motion capture system.

Joint angle and torque estimations were performed using a standard, planar inverse dynamics method [5] using the kinematic data measured from motion capture and the GRFs recorded from the force plates. The position of the markers, coupled with simple trigonometric relationships, can calculate the angle of the joint. Torque in the ankle is calculated from the GRF measured by the load cells under the subject’s foot. Subsequently, the torques at the remaining joints can be estimated by multiplying the force of the previous joint by the distance between them.

All software and data used have been made available ([31], Github Repository, 2015, DOI: 10.5281/zenodo.13030).

## 2.2 Compensation of Inertial Artifacts

Horizontal acceleration of the ground surface is commonly used in experiments to perturb posture and gait [32, 33]. In order to determine joint moments during such tests, GRFs must be measured, but this is problematic when the force plate is not rigidly attached



Figure 2.2: The treadmill with coordinate system, cameras (circled in orange), projection screen, and safety rope.

to an inertial reference frame. In an accelerating force plate, inertial forces arise due to accelerating masses between the subject's foot and the force sensors. Compensation for these errors in a translating force plate is possible when mass properties of the plate are known and accelerations are measured [34].

Instrumented treadmills are increasingly available as tools for gait analysis, and these provide a convenient means to apply horizontal surface acceleration during posture and gait [35, 36]. It is expected, however, that acceleration of the treadmill belt will induce a sagittal plane moment in the GRF due to the inertia of the belt, rollers, and motor (Figure 2.3). This moment is an artifact which will directly translate into an error in the sagittal plane joint moments determined from inverse dynamic analysis. Similar errors may occur when belt speed is interactively controlled ("self paced") by the subject in a virtual reality environment [37]. In this section, we will quantify the inertial artifacts caused by belt speed variations and present a method to compensate for these artifacts [38].

A linear, second-order discrete-time model was used to predict the pitch moment  $M$  from belt acceleration  $a$ :

$$M_i = \theta_1 M_{i-1} + \theta_2 M_{i-2} + \theta_3 a_i + \theta_4 a_{i-1} + \theta_5 a_{i-2} \quad (2.1)$$

Before applying this method to the human perturbation data, a separate set of test conditions quantified the effectiveness of the linear model in reducing inertial errors. Input signals for controlling the belt velocity were created using the same MATLAB Simulink method shown in Figure 2.1. A total of four, 6-minute trials were generated, two with mean speed of 1.2 m/s and small perturbations, and two with a mean speed of 2.0 m/s and larger perturbations. A random acceleration signal was generated with discrete-time Gaussian white noise and variance in the acceleration was set to 25 m<sup>2</sup>/s<sup>4</sup> (for the 1.2 m/s trials) and 2000 m<sup>2</sup>/s<sup>4</sup> (for 2.0 m/s trials), respectively.

The signal was clipped at the maximum belt acceleration of 15 m/s<sup>2</sup>, integrated, and

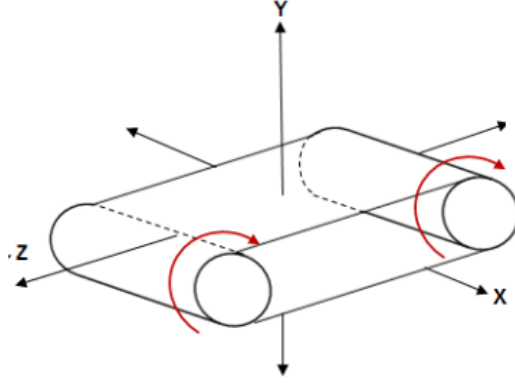


Figure 2.3: A diagram of the treadmill with coordinate system, where the red arrows describe the rotation of the treadmill roller which will introduce errors in pitch moment in measured ground reaction forces ( $M_x$ , in this system)

high-pass filtered (second-order, Butterworth) with a 0.2069 Hz passband edge frequency to eliminate any velocity drift. The mean velocity was added as a constant to the random signal and limited to a maximum speed of 3 m/s. Two trials were generated in this manner for each speed, using different random number seeds, to guarantee the belt motions of the two trials were different from each other. The resulting belt velocity signals had a mean and standard deviation of  $1.20 \pm 0.10$  m/s and  $2.00 \pm 0.50$  m/s, respectively.

The recorded pitch moment and belt speed were low-pass filtered (second-order, Butterworth) with a 6 Hz cutoff frequency to simulate how signals are typically processed for inverse dynamic analysis of gait [39]. Belt acceleration was derived from the low-pass filtered belt speed by a central difference formula.

One trial at each speed was used to calibrate the model. The five model coefficients  $\theta$  were determined by minimizing the sum of the squared error between the predicted and measured pitch moment in the calibration trial. The minimization was performed in MATLAB using the *fmincon* function:

$$M = \operatorname{argmin}_{\theta} \sum \|M_{\text{measured}} - M_{\text{predicted}}\|^2 \quad (2.2)$$

The calibrated model was used to predict the pitch moment of the other trial at the same speed, and the predicted moment was subtracted from the recorded moment as would be done when compensating the GRFs of the perturbation experiments:

$$M_{\text{compensated}} = M_{\text{measured}} - M_{\text{predicted}} \quad (2.3)$$

The root-mean-square (RMS) of the uncompensated and compensated pitch moment were computed. The coefficient of determination ( $R^2$ ) verified the predictiveness of the simulation when compared to the measured values.

For the perturbation experiments, the compensation model was calibrated using an unloaded treadmill without a test subject, recorded the same day of the experiment.

All software and data used have been made available ([40], Github Repository, 2014, DOI:10.5281/zenodo.10905).



## 2.3 Results

The pitch moment predicted by the model was in close agreement with the measured pitch moment, as illustrated in Figure 2.4. The predicted moment was generated after calibrating the model using data from the other random trial at the same speed.  $R^2$  values of 72.08% and 96.75% were obtained for the slow speed (1.2 m/s) and fast speed (2.0 m/s), respectively, and indicate that the model explains most of the pitch moment that is generated by belt speed variations.

Table 2.1 shows the RMS values of pitch moment before and after compensation. Substantial reductions in error were achieved, especially in the high speed condition.

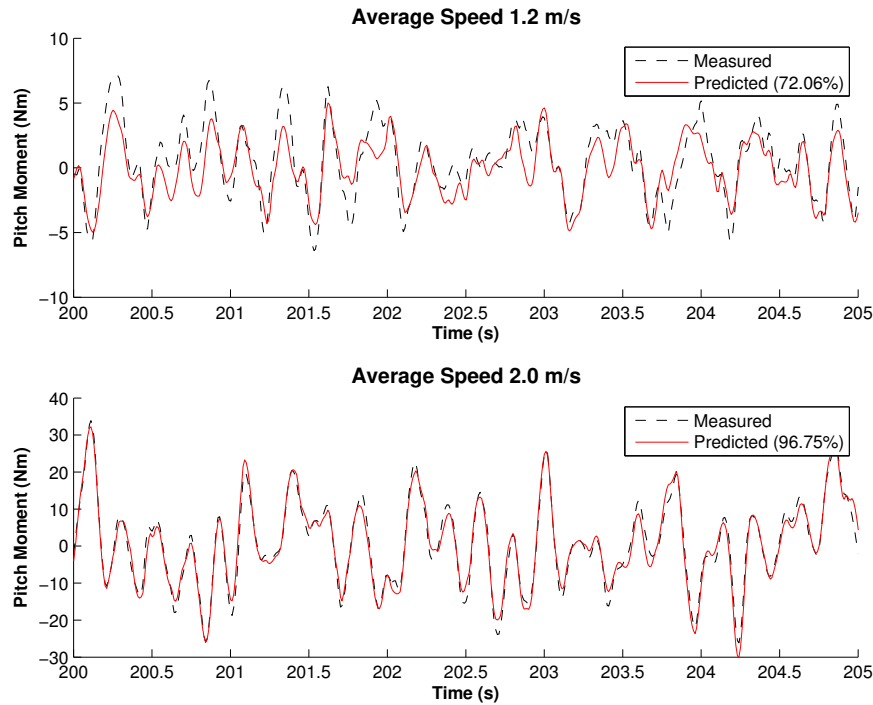


Figure 2.4: Measured (black dotted) and predicted (red) pitch moment for the slow (top) and fast (bottom) speeds, with  $R^2$  values of 72.08% and 96.75%, respectively. Only a small section of the 6-minute trial is shown.

Trial	RMS (Nm)		% Reduction
	Before Compensation	After Compensation	
Low Speed (1.2 m/s)	2.77	1.46	47.37
High Speed (2.0 m/s)	11.51	2.07	81.98

Table 2.1: Root-mean-square (RMS) of the pitch moment before and after compensation. Compensation was performed by subtracting the predicted pitch moment from the measured value.

Sagittal plane moment between the foot and ground is one of the inputs for inverse

dynamic analysis of human motion. Inspection of the inverse dynamic equations reveals that any measurement error in this moment will result in an equal error in human joint torques. Peaks in the inertial artifacts during our tests were typically 6 Nm in the slow condition and 30 Nm in the fast condition (Figure 2.4). Peak knee joint torques during human gait are about 40 Nm during slow walking [39], so these inertial artifacts are large. We were able to reduce this error by about half. Our slow condition is representative of an experiment in which gait is perturbed just enough to cause subtle adaptive responses, similar to the perturbation experiments described in Section 2.1. In more extreme perturbations, such as sudden stopping or starting of the belt, the inertial artifacts would be larger, and as indicated by our fast tests, a much larger fraction of the artifact can be compensated in these conditions.

Therefore, this method adequately reduced inertial artifacts in the joint torque calculations from the perturbation experiments. Included in the protocol described in Section 2.1, each walking trial included a corresponding, unloaded trial where the treadmill experienced the same perturbations without a test subject walking on the belts. These unloaded trials were used to calibrate the model and remove the inertial errors in the trial of the same movement with the test subject. Then, the joint angles and joint torques were calculated using inverse dynamics and the compensated GRFs. Fewer errors ensure the tuning of the reflex control will relate to actual human responses and not inertial measurement errors.

## 2.4 Status and Contribution

The design of the perturbation experiments, the development of the compensation method, and all experimental tests have been completed. A data set of perturbation experiments was published [30], as well as the compensation method [38]. Previously, no method existed for compensating the inertial errors induced by varying the belt speed of an instrumented treadmill. Due to the prevalence of perturbation studies, this technique allows for a more accurate calculation of joint torques through inverse dynamics when subjected to similar mechanical perturbations.

Additionally, the published data set, complete with seven and a half hours of walking data, benefits the biomechanics community. This allows any researcher in the field to develop and verify other mathematical models using the data we collected.

# Chapter 3

## Development of a Virtual Muscle Model

Human motion is dictated by a neural control signal sent from the brain which contracts the muscle and produces joint movements [1]. A more muscle-like actuation system may be capable of better replicating able-bodied locomotion in powered prosthetic devices or exoskeletons. The biarticular nature and nonlinear viscoelastic and dynamic properties of muscles could simplify feedback control and improve performance. It has been shown through simulation that muscle properties contribute substantially to stability during walking when compared to torque-driven control [9]. This is because the passive, springlike properties of muscles prohibit unnatural behaviors arising from unstable torque commands.

This section details the selection of a muscle model capable of achieving accurate simulations of muscle dynamics in real-time. The muscle model is detailed in Section 3.1, while the approach for simulating and evaluating its accuracy and computation speed are outlined in Section 3.2. The results of the model validation study and the accuracy/speed tests are summarized in Section 3.3.

### 3.1 Musculotendon Model

A muscle-driven controller relies on both biologically accurate and computationally fast simulations of muscle dynamics. Generally, musculotendon models are divided into two separate categories: cross-bridge models and Hill-type models. Though cross-bridge models describe the biological function and structure of muscles [41, 42, 43], the number of parameters renders computation time both impractical and unfeasible for real-time use in prosthetic devices [44]. Other muscle methods accurately describe the biological properties of cross-bridge models, though they are computationally demanding [45, 46, 47]. Alternatively, Hill-type muscle models are widely used in muscle-driven simulations of human movement [48, 49]. Due to its widespread use, this proposal will focus on the classic structure of Hill-models.

The primary feature of Hill-type models centers around a contractile element (*CE*) governed by forces due to the myosin and actin cross-bridge at the sarcomere level of muscles. Different from other cross-bridge models, the complexity of muscle contraction is simplified by assuming general force-length and force-velocity relationships exhibited by muscles [50],

which were estimated through experiments conducted by Hill [51]. An example of these force-length and force-velocity relationships is shown in Figure 3.1.

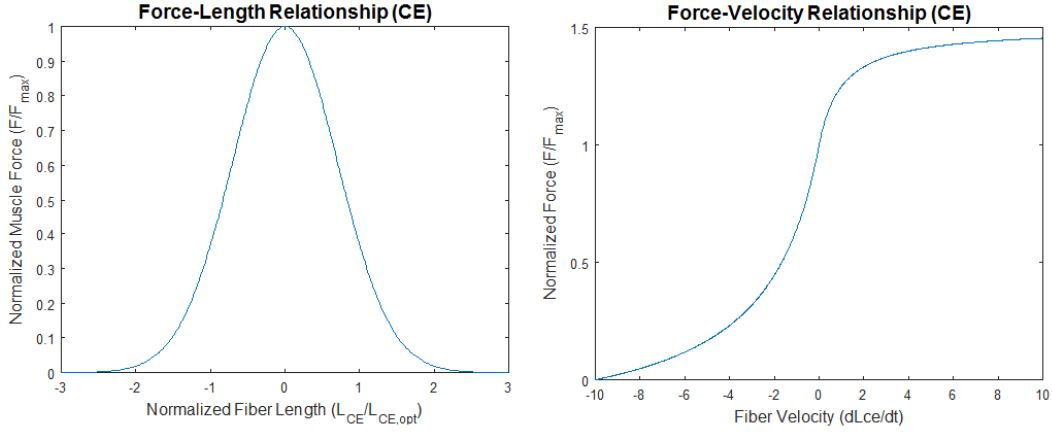


Figure 3.1: Standard force-length (left) and force-velocity (right) of the contractile element (CE) in Hill-type muscle models, where negative and positive velocities represent shortening and lengthening, respectively

The remaining elements of the Hill-type models are the parallel and series elastic elements (*PEE*, *SEE*), modeled as nonlinear springs. The *PEE* represents the passive, connective tissues surrounding the contractile element, while the *SEE* represents the tendon joining the muscle and bone. When the *CE* is not activated, the springlike behavior of the *PEE* and *SEE* ensure the passive dynamics of muscles are preserved.

Nonlinear properties in these passive elastic elements arise from the inability to produce force until the slack-lengths of the *PEE* and *SEE* are superseded by the length of the muscle. However, after the muscle length is longer than the slack-length, the force contribution becomes a quadratic relationship of the difference between the current muscle length and the slack-length.

Additional simplifications to Hill-type models include representing muscle fiber geometry as perfectly parallel fibers of equal length and constant muscle volume [44]. The attachment angle of the fiber to the tendon is defined by the pennation angle ( $\phi$ ), which guarantee that the muscle fibers attach at a consistent height. For numerical stability in muscle-driven simulations, a small amount of viscous damping can be added in parallel to the contractile element. An illustration of a classic three-element Hill-type model with pennation angle and damping element is shown in Figure 3.2.

Using this muscle architecture, activation and contraction dynamics can be represented as a set of two differential equations, where the state variables are the length of the contractile element ( $L_{CE}$ ) and the muscle activation signal ( $a$ ). Activation dynamics are driven by neural excitation signals ( $u$ ) from the brain or spinal cord:

$$\dot{a} = (u - a) \left( \frac{u}{T_{act}} - \frac{1 - u}{T_{deact}} \right) \quad (3.1)$$

where  $T_{act}$  and  $T_{deact}$  are the the time constants of muscle activation and deactivation, respectively.

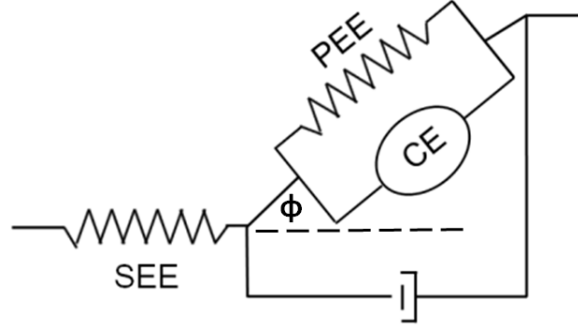


Figure 3.2: Typical three-element Hill-type muscle model, consisting of a contractile element ( $CE$ ), parallel and series elastic elements ( $PEE$ ,  $SEE$ ), pennation angle ( $\phi$ ) and viscous damping in parallel to the  $CE$

Subsequently, the overall force in the muscle ( $F_{SEE}$ ) can then be calculated based on the individual force contributions of the three elements of the Hill-type muscle model:

$$F_{SEE} = \left( a \cdot F_{max} \cdot f_{FL}(L_{CE}) \cdot f_{FV}(\dot{L}_{CE}) + F_{PEE} \right) \cos \phi + F_D \quad (3.2)$$

where  $F_{max}$  is the maximum isometric force of the muscle,  $f_{FL}$  and  $f_{FV}$  are the force-length and force-velocity relationships, respectively, and  $F_{PEE}$  and  $F_D$  are the force contributions due to the  $PEE$  and damping element. The additional mathematical relationships of the muscle model can be referenced in Appendix B.

For use in a prosthetic device or exoskeleton, the muscle model must perform all calculations at least as fast as real-time. However, the differential equations that describe muscle dynamics are stiff and highly nonlinear. In variable step methods, these nonlinearities require small simulation time steps, thereby prohibiting real-time application. Recently, a fixed-step, implicit formulation of musculoskeletal dynamics was developed [26, 52, 53] to eliminate the mathematical singularities which can stifle computation time.

Using this method, the muscle activation (3.1) and contraction (3.2) relationships can be combined into a single, implicit state equation:

$$f(x, \dot{x}, u) = 0 \quad (3.3)$$

with state variables  $x_n = [L_{CE} \ a]^T$  and state derivatives  $\dot{x}_n = [\dot{L}_{CE} \ \dot{a}]^T$ , where  $n$  is the number of muscles. The control inputs,  $u$ , are the neural excitation control signals generated by the reflex controller (Section 4, Appendix D). This implicit formulation of forward muscle dynamics can be solved using a fixed-step, linear, first-order Rosenbrock solver. Details of the Rosenbrock method can be referenced in Appendix C.

## 3.2 Muscle Simulation and Evaluation

The muscle model must be tested in simulation to observe if realistic forces are produced under a prescribed muscle activation. Therefore, we used a planar leg model with three

monoarticular muscle groups (Vasti, Soleus, Tibialis Anterior) and three biarticular groups (Rectus Femoris, Hamstrings, Gastrocnemius) to simulate the muscle model. The values of the muscle parameters were obtained through prior experiments reported in literature [54]. Inputs to this model are neural excitation signals ( $u$ ) and musculotendon length ( $L_m$ ) derived from joint angles (hip, knee, and ankle) obtained through motion capture and inverse dynamics (Section 2.1). The torque at each joint ( $\tau$ ) can be calculated by multiplying the force ( $F_{SEE}$ ) generated by each muscle ( $i$ ) with the moment arms ( $d$ ):

$$\tau_{joint} = \sum_i d_{joint,i} F_{SEE,i} \quad (3.4)$$

Figure 3.3 is an overview of the VMR controller, including the inputs and outputs of the muscle model. When implemented on a prosthesis or exoskeleton, the inputs to the muscle model will be obtained from hardware components, including encoders and force sensors, and the torque output from the muscle model will drive the electric motors.

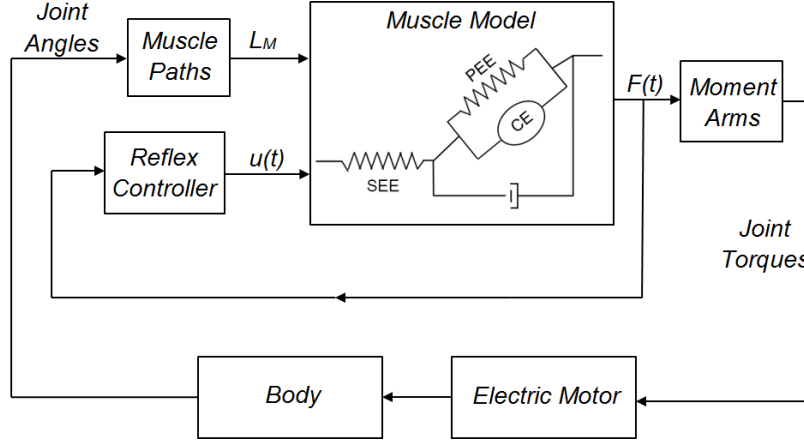


Figure 3.3: Overview of the Virtual Muscle Reflex (VMR) controller, where the inputs to the model are the muscle length  $L_m$  and neural excitation signal  $u$ , and the output is the muscle force which can be multiplied by the moment arm to obtain the joint torque

Two separate test cases were performed to verify that the muscle model produces reasonable muscle forces and joint torques.

**Model Evaluation.** The first test evaluated the feasibility of the model, where joint angles were held constant at  $0^\circ$  while a step-control fully actuated each muscle at different times throughout the simulation (Figure 3.4). Observing the corresponding force in each muscle and torque in each joint indicates if the model behaves appropriately when certain muscles of the leg are activated. For instance, activating a muscle in the posterior of the leg will produce joint torques in the appropriate direction, while activating a muscle in the anterior of the leg will influence joint torque in the opposite direction. For biarticular muscles, this torque will effect every joint in the muscle path.

**Speed and Accuracy.** A second test condition evaluated the performance of the model and Rosenbrock solver by calculating the accuracy of the model and the computation time.

To mimic the cyclic nature of a regular human gait cycle, joint angle time histories  $q(t)$  for 30 seconds of normal walking and 1 Hz sinusoidal test signals for the muscle excitations  $u(t)$  were used in the simulation. However, the muscles in the anterior and posterior of the leg were activated out of phase, to represent the maximum torque which could ever be produced by the model (Figure 3.4). Simulations were performed in MATLAB using fixed time steps ranging from 0.08 to 16.0 ms. Numerical simulation errors were quantified as a percentage of the maximum joint torques compared to the result from the smallest time step, which was considered to be the most accurate. Computation times were measured in all tests.

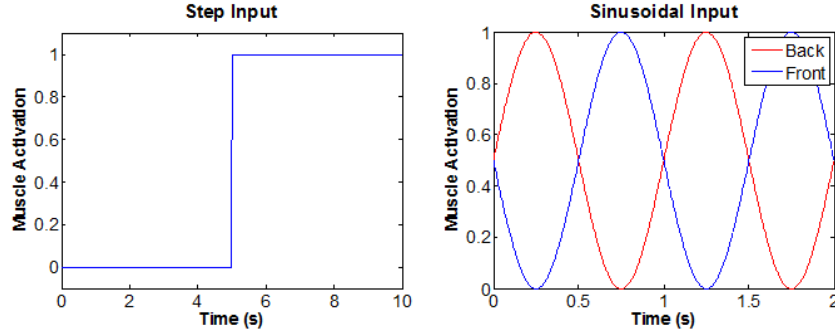


Figure 3.4: Step-input signal for the muscle model validation (left) and sinusoidal input signals with 1 Hz frequency (right) for evaluating the speed and accuracy of the model

Initially, the muscle model was programmed in MATLAB when the speed and accuracy tests were first performed. However, for even faster computation times, the VMR system was reformulated in the C programming language and compiled as a MEX function to be run in the MATLAB pipeline. The simple formulation of muscle dynamics (see Appendix C) allows for the equations to be directly implemented in the low-level programming environment typically used in the microcontrollers. The output torque and muscle models of both the MATLAB and C-MEX functions were compared to ensure the models were equivalent.

### 3.3 Results

Two test cases evaluated the performance of the musculotendon model. First, the results of the predicted muscle forces and joint torques produced by the model given a step-input neural excitation command are shown in Section 3.3.1. Subsequently, the results of the speed and accuracy tests are shown in Section 3.3.2, where 30 seconds of joint angle time histories and sinusoidal muscle excitations represented the most extreme scenario for the muscle model to perform.

#### 3.3.1 Model Evaluation

The muscle forces and joint torques obtained through the model responded appropriately to the prescribed muscle excitations. Figure 3.5 demonstrates the first test case where joint angles were held constant at  $0^\circ$  while a step-control fully actuated each muscle at

random times throughout the simulation. Predicted torques in the knee (blue) and ankle (green) correspond as expected to the muscle activations in the thigh and shank. The torque directions in the knee and ankle are influenced by muscle activations in the anterior and posterior of the leg. Additionally, the biarticular properties of muscles are represented when the gastrocnemius (cyan) is activated, in which both the knee and ankle torques are affected.

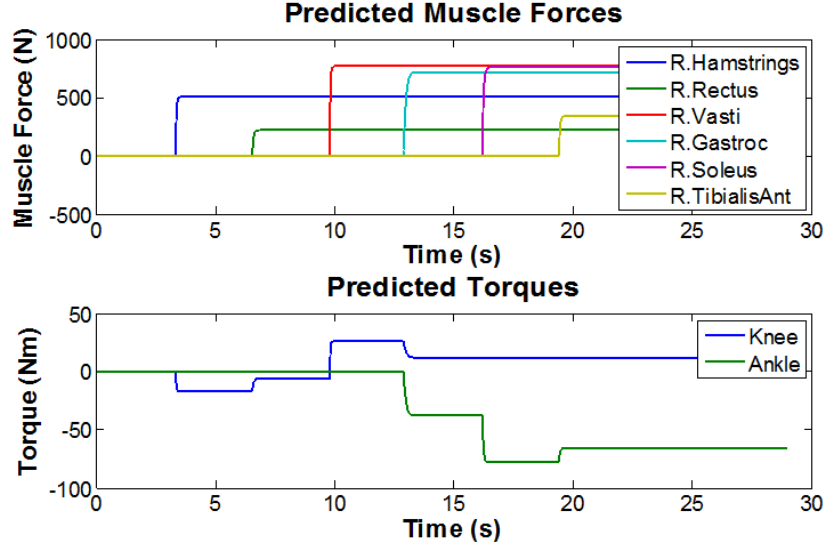


Figure 3.5: Predicted muscle forces (top) and torques (bottom) with constant joint angles  $q(t)$  held at  $0^\circ$  and step-control signal  $u$  randomly applied throughout the simulation.

### 3.3.2 Speed and Accuracy

The speed and accuracy of the muscle model was evaluated using joint angles from walking data and sinusoidal input signals. Intuitively, the results depended on the integrator step size, as shown in Figure 3.6. In MATLAB, real-time is achieved at step sizes as small as 0.18 ms with simulation errors below 1%, indicated by the dashed red line. Though larger time steps still produce acceptably accurate results, the model became unstable for time steps larger than 16 ms.

When reprogrammed in a C-MEX function, the computation time decreased by a factor of over 100, thereby allowing for faster convergence in optimizations (see Section 4.2). For example, an optimization using the an extremely small timestep of 0.001 ms can solve the 8 minute walking within real-time, as shown in Figure 3.7.

Therefore, the VMR system, including the both the muscle model and the spinal reflexes, can obtain accurate results at extremely fast computation times. Using a reasonably accurate step size of 0.18 ms, 8 minutes of walking data can be simulated in just 0.058 seconds. This speed is more than sufficient for real-time hardware applications.



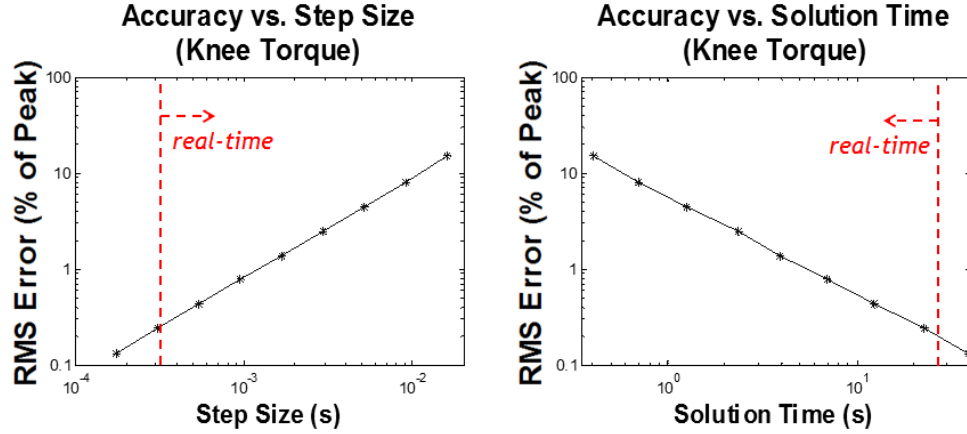


Figure 3.6: Accuracy is effected by the integrator step size (left) and computation speed (right). Error was quantified as a percentage of the maximum moments in the knee and ankle. Real-time is indicated by the dashed red line, which is faster than 30 seconds. These results indicate that torques can be obtained in a simulation of muscle dynamics with accurate results and minimal computation time.

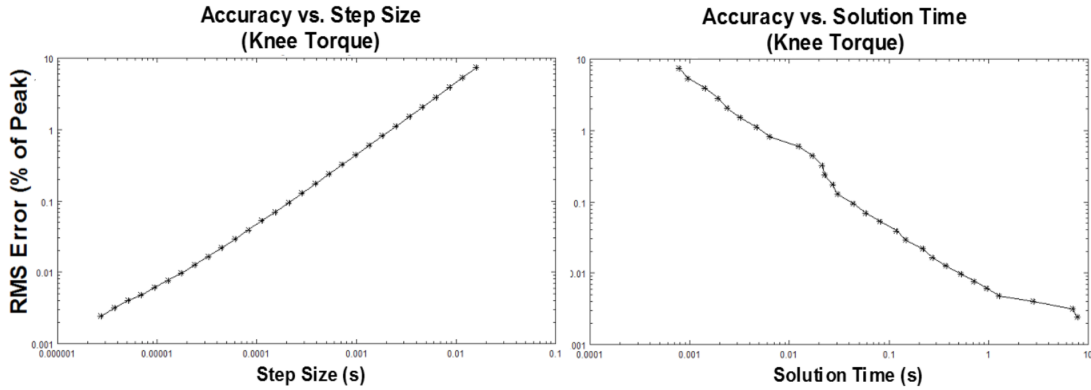


Figure 3.7: Accuracy vs. step size (left) and computation speed (right) using the VMR system in the C-programming language. All step sizes achieved real-time results, including an extremely small step size of 0.001 ms

### 3.4 Status and Contribution

The selection and development of the muscle model, as well as all testing, has been completed. The model produced reasonable forces and joint torques given the prescribed muscle activations. Additionally, the model is highly accurate and solves well within the range of real-time requirements. Though an implicit formulation of muscle dynamics was previously derived [26], rewriting these equations into a simple linear form had not yet been performed or tested. The neuromuscular reflex controllers currently used in prosthetic devices [21, 23] are simplified equations that cannot capture the full stabilizing benefits of muscle dynamics. This new formulation allows a more accurate representation of muscles that can be programmed in microcontrollers.

# Chapter 4

## Virtual Muscle Reflex (VMR) Control, Optimization, and Statistical Analysis

The neural excitation signals which drive the muscle dynamics are generated by muscle reflexes described in Section 4.1. In current applications, reflex controllers are tuned manually until walking is achieved in simulation studies [20, 22]. However, the parameters of the controller can be tuned through optimizations which minimize the difference between the torque exhibited by test subjects and the torque produced by the VMR system. The optimization techniques are described in Section 4.2. Lastly, to quantify if reflexes can describe normal walking and can reproduce the variation within and between gait cycles, a statistical analysis will be performed (Section 4.3). Preliminary results of the optimization are summarized in Section 4.4.1 and Section 4.4.2, with statistical analysis results in 4.4.3.

### 4.1 Neuromuscular Reflex Controller

The autonomous, positive force feedback reflex controller of Geyer and Herr will be exclusively used in the VMR system [20]. Though positive force feedback is typically avoided in most classical control applications, studies in both animals and humans suggest that positive force feedback increases stability in walking and running [55, 56]. Positive force feedback manifests itself as a stabilizing mechanism in response to the activity of other muscles [57, 58].

In general, spinal reflexes modulate between the innervation of flexor/extensor muscles and the inhibition of the corresponding extensor/flexor muscle [1]. For instance, the natural reflex from stepping on a sharp object involves the innervation and inhibition of extensor/flexor muscle pairs in the both legs. Therefore, it can be assumed that the same strategies exist during other movements which require constant stabilization, including walking.

With positive force feedback, the reflex equations are a simple sum of the muscles pre-stimulation ( $S_m$ ) and a time-delayed force ( $F_m$ ) multiplied by a gain ( $G_m$ ). For example, the stance phase equation for the Soleus muscle can be written as:

$$u_{SOL} = S_{0,SOL} + G_{SOL}F_{SOL}(t - t_{SOL}) \quad (4.1)$$

However, to avoid hyperextension of the joints and to guarantee postural stability and smooth movements during the swing phase, these equations become increasingly more complex. Separate sets of equations for both the swing and stance phase are required for each muscle group and require more sensory information, such as the tilt angle of the torso and force in the contralateral and ipsilateral leg. For brevity, the full details of the reflex model can be referenced in Appendix D.

In order to differentiate between the swing and stance phases of walking, a simple threshold control was added to the reflex model. If the GRF is above 10 N, then the leg is considered to be in stance phase. This threshold was selected to prevent the interference of measurement noise in the force plates. In a prosthetic device or exoskeleton, a force sensor will need to be added to the hardware in order to regulate the switching between the swing and stance controllers.

First, we will consider only the ankle reflex controller used in the BiOM (BionX Medical Technologies, Inc., Bedford, Massachusetts, USA, [21]). In the preliminary investigation, we will tune the ankle reflexes of the VMR system by using a lower-limb model of the leg (Soleus, Tibialis Anterior, and Gastrocnemius). After this controller produces reasonable joint torques in the ankle, the VMR system will be expanded to include the more complicated reflexes and PD control of the hip and knee joints. For testing, the leg model will then be expanded to include muscle groups in the upper leg (Vastus, Hamstrings, and Gluteus).

## 4.2 Optimization

Spinal reflex models and virtual muscles have been successfully demonstrated in simulation, but have not been compared to human control actions [20, 21, 22]. Typically, the parameters of these reflex controllers are manually tuned until cyclic, human-like walking is observed in a simulation model. However, the ability of these controls to mimic actual human movements obtained from experiments have not yet been explored. Here, we investigated the possibility of using the VMR system in order to determine if muscle reflexes are capable of reproducing able-bodied walking. This can be accomplished by minimizing a cost function through optimization methods. Using the perturbed human walking gait data (see Section 2.1), the parameters of the reflex controller (Section 4.1) can be tuned through an optimization, illustrated in Figure 4.1.

In mathematics and computer science, optimization methods can find the best parameters in a set of mathematical equations which either minimize or maximize a given cost function [59]. In this proposal, the aim is to adjust the parameters in the reflex controller to minimize the difference between the torque generated by the VMR model and the measured torque from the human perturbation experiments.

In cases of complicated, nonlinear equations, such as muscle dynamics and reflexes, many optimization methods struggle to find the best solution from a wide range of possible solutions, or local minima. Several methods have been developed which aim to avoid local minima and discover the global minimum, or best solution. These strategies involve cleverly manipulating the search space to more adequately guarantee model convergence. Recent methods for improving model convergence include direct collocation [60], homotopy methods [61], biogeography-based optimization [62], and covariance matrix adaption [63].

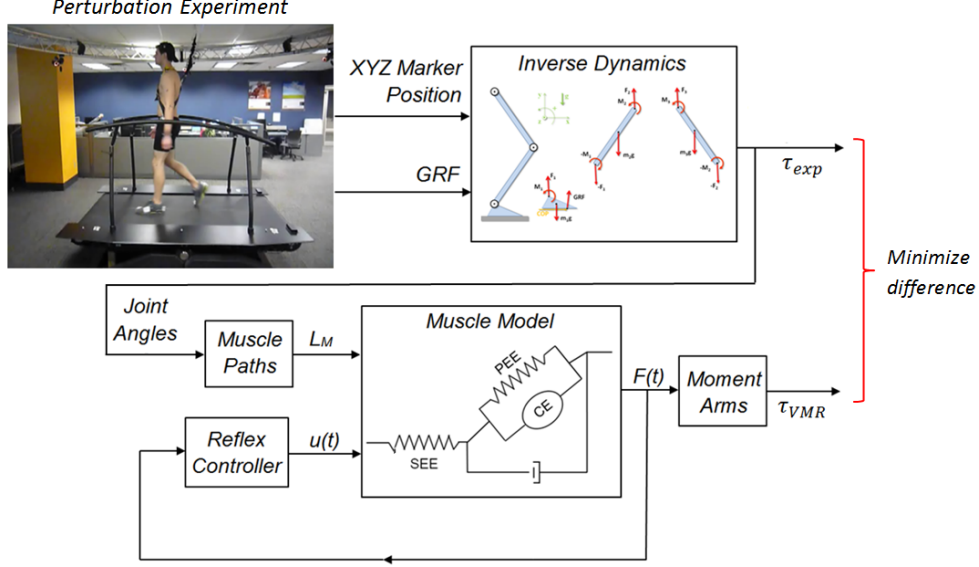


Figure 4.1: The parameters of the VMR system can be determined by minimizing the difference between the torque obtained through the experiment and inverse dynamics,  $\tau_{exp}$ , and the torque produced by the neuromuscular reflex model  $\tau_{VMR}$

The Particle Swarm Optimization (PSO) population-based method was used as the optimization algorithm due to its simplicity and adaptability to the VMR system [59]. PSO algorithms use a population, or swarm, consisting of possible solutions, called particles. In each iteration, the best solution from generations of particles dictates the movement of the swarm. After several generations, the algorithm converges to a feasible solution.

The control parameters were optimized in MATLAB using a PSO algorithm and a multi-objective cost function. The tracking term of the cost function minimized the norm between the ankle torque produced by the VMR system ( $\tau_{VMR}$ ) and measured ankle torque from the 8 minutes of perturbed walking data ( $\tau_{exp}$ ). The effort term was modeled as the mean of the squared muscle activation ( $a$ ):

$$C = W_1 \left( \frac{1}{N} \sum \sqrt{(\tau_{VMR} - \tau_{exp})^2} \right) + W_2 \left( \frac{1}{N} \sum \sqrt{a^2} \right) \quad (4.2)$$

where  $W_1$  and  $W_2$  are the weights for the tracking and effort terms, respectively. Without the effort term, optimization techniques tend to discover unrealistic solutions where one muscle produces the entire movement. The effort term forces every muscle to contribute to the motion.

In addition to the 8 control parameters of the ankle reflex controller (see Appendix D.1), muscle properties including the *SEE/PEE* slack-lengths and reflex time delays for each muscle were selected as parameters in the optimization. These muscle properties are influenced by the gain and delay parameters in the reflex model, which may unrealistically increase the amount of force produced by the muscle, as well as effect the timing of muscle activation. Because muscle models are sensitive to the nonlinearities of the *SEE* and *PEE* elements, slack-lengths and delays must be included in the optimization to ensure the muscle

can produce force at the correct time.

However, to achieve better optimization results, it may be beneficial to include less obvious muscle properties among the optimization parameters [64]. All muscle properties were individually added as parameters in the optimization, where the RMS between the torque produced by the model and measured from the experiment was calculated.

As some variability exists in PSO algorithms, the optimization was repeated 10 times for each parameter, where the mean and standard deviation of the RMS across all trials was calculated. The mean RMS value of the 10 trials of each new parameter was compared to the mean RMS of the original parameters (8 reflex control parameters, slack-lengths, and delays). If the addition of the parameter significantly reduced the RMS error, the new parameter would be included in the optimization. Details concerning the other muscle properties of interest can be referenced in Appendix B.

The initial guess for the optimization was the original reflex control parameters reported by Geyer and Herr [20] and the muscle parameters used in previous literature [54]. The convergence of the optimization was determined by plotting the change in the objective function throughout each iteration of the algorithm, in which an example is shown in Figure 4.2. The population of the swarm and the number of nearest neighbors in the PSO algorithm can be adjusted until the objective function no longer changes. Additionally, the number of generations can be adjusted if convergence has been achieved earlier in the optimization, or lengthened if the objective function is still being minimized.

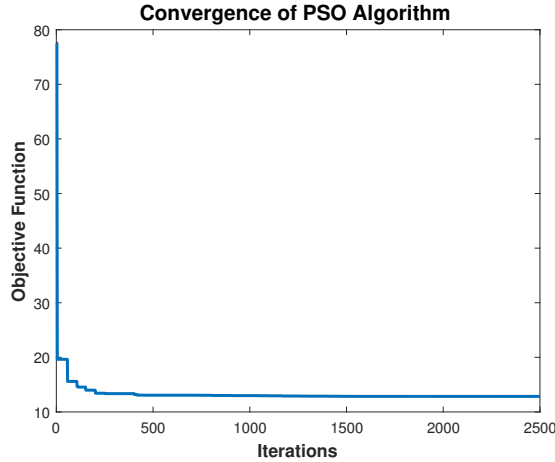


Figure 4.2: The change in objective function as a function of the number of iterations of the optimization algorithm. In this example, the number of generations should be lowered to reduce the computation expense of the optimization

The parameters identified through the optimization will be used to generate the reflex control signals,  $u(t)$  which drive the virtual muscles of the VMR model. Using joint angle time histories from the 8 minutes of walking data, the torque from the experiment and the VMR system can be compared.

## 4.3 Statistical Analysis

To understand the capabilities of the VMR system in describing both variations in a normal gait cycle and its ability to respond to external perturbations, a statistical analysis must be performed on the optimized VMR system. Joint angle time histories of the 8 minute perturbed walking trials will be used as input to the VMR system. After the optimization identifies the values of the parameters, the predicted joint torque will be statistically analyzed.

As each gait cycle contains reactive responses to random perturbation signals, an average of all gait cycles would eliminate the crucial information that can help identify the human controller. Instead, each gait cycle was split into 100 different points, separated by the time of heelstrike and toe-off. For 8 minutes of walking data, there will be 480 gait cycles. For each of these 100 points, the coefficient of determination ( $R^2$ ) was calculated in order to correlate the predicted and measured joint torque across all cycles for a given instance in the gait cycle. For instance, if the highest  $R^2$  value occurs at 50% of the gait cycle, it would indicate that the VMR system most accurately describes the peak joint torque in the ankle, which typically occurs at this time. Poor  $R^2$  would suggest the VMR system cannot describe that particular instant of the gait cycle.

Subsequently, a regression line can be fit from the measured torque plotted against the predicted torque [65]. Areas of the gait cycle with poor fit will also indicate that the VMR could not adequately describe this portion of the gait cycle. Lastly, the mean of the measured and predicted torque can be calculated and plotted against each other to visually assess how well the VMR system performed at each point in the gait cycle.

## 4.4 Results

In this section, we present an example of the results obtained from the optimizations and statistical analysis of one subject and one trial (male, age = 22, mass = 81 kg, speed = 1.2 m/s). First, the results for determining which muscle parameters to include in the optimization are shown in Section 4.4.1. In Section 4.4.2, the optimized VMR system predicted the joint torque from the joint angles of the 8 minute perturbation trial. Lastly, the statistical analysis are shown in Section 4.4.3, to quantify how well the torque produced by the model fits the torque exhibited by the test subject.

### 4.4.1 Muscle Parameter Selection

To readily identify which muscle parameters are essential to the performance of the VMR system, 10 trials of optimizations were performed for each muscle parameter in addition to the original set (8 reflex control parameters,  $SEE/PEE$  slack-lengths, and neural signal delays). Table 4.1 summarizes the results of these trials, in which the mean and standard deviation of the 10 trials are shown.

In most cases, adding parameters does not substantially contribute to the performance of the VMR system when compared to the original parameters. Some parameters, including the maximum isometric force,  $F_{max}$ , and maximum contraction velocity,  $V_{max}$ , increase the error

Parameter	<i>Orig.</i>	$F_{max}$	$L_{ce,opt}$	<i>Width</i>	<i>Mom.Arm</i>	$u_{max}$	$V_{max}$	$T_{act}, T_{deact}$
<b>Avg.</b>	1.69	1.72	1.53	3.13	1.57	1.03	3.77	1.67
<b>STDEV</b>	0.61	0.53	0.47	1.1	0.38	0.40	0.85	0.34

Table 4.1: The mean and standard deviation of the RMS difference between the experimental and predicted torques, using several different muscle parameters in the optimization

between the measured and predicted torques. This is because several muscle parameters are redundant between the virtual muscles and reflexes, such as the gained force in the reflex and  $F_{max}$ . Too many optimization parameters increases the complexity of the control, preventing timely convergence in the PSO algorithm. In the case of  $V_{max}$ , the model had difficulty converging to a solution, as indicated by the larger standard deviation. Lastly, any marginal improvement in the RMS error are not worth the increase in computation time.

However, a significant reduction in error can be observed in  $u_{max}$ , which affects the stiffness in the  $SEE$  in relation to  $F_{max}$ . Therefore, this was the only additional parameter added to optimization.

Using this set of optimization parameters, the settings of the PSO algorithm were set to a generation = 50, population = 50, and neighbors = 20. These definitions ensured the model converged in a timely fashion.

#### 4.4.2 Ankle Joint Torque

The results of the optimization suggest that muscle reflexes alone can generate realistic joint moments for use in a prosthetic device. Data from one test subject (male, age = 22, mass = 81 kg, speed = 1.2 m/s) is shown in Figure 4.3, where the experimental (black) and VMR (red) ankle torque are compared.

The VMR system produces variations in peak moment between gait cycles and the majority of these variations correlate to the torque observed in the subject. The predicted joint torque matches the amplitude and timing of ankle push-off and mimics the shape of the experimental torque during the swing phase. Some of the discrepancies between the experimental and predicted joint moment during the swing phase may be attributed to residual errors after performing the inertial compensation on the GRF (see Section 2.2).

It is important to note that reflexes alone are not responsible for human locomotion. A combination of CPGs and other cognitive processes, including visual, vestibular, and sensory feedback, also contribute to the human control strategies. Though our results suggest that an autonomous reflex controller is capable of explaining a majority of human response actions, a reflex model that perfectly tracks joint torque trajectories is not feasible in practice. Since reflexes are reactive, additional control may be required to precipitate motion. However, the Indego exoskeleton is equipped with a trunk lean angle which may be enough to trigger plantarflexor force feedback and produce locomotion.

#### 4.4.3 Statistical Analysis

Data from one test subject (male, age = 22, mass = 81 kg, speed = 1.2 m/s) is shown in Figure 4.4, in which the mean predicted and measured joint torque is plotted as a function

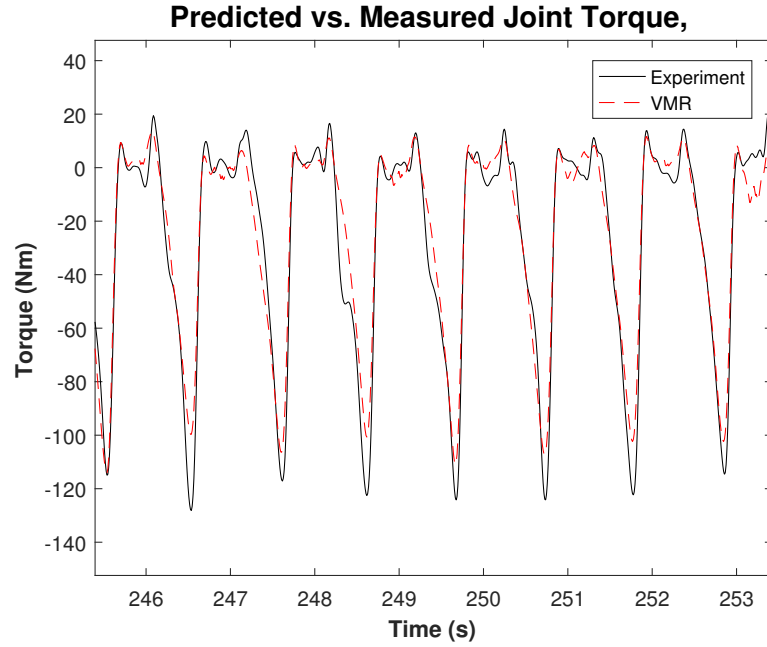


Figure 4.3: Measured (black) and predicted (red dashed) joint torque, zoomed to only a few seconds of the 8 minute walking trial, for clarity. Note that negative torque corresponds to ankle plantarflexion

of the gait cycle. On average, the VMR system outputs the correct torque.

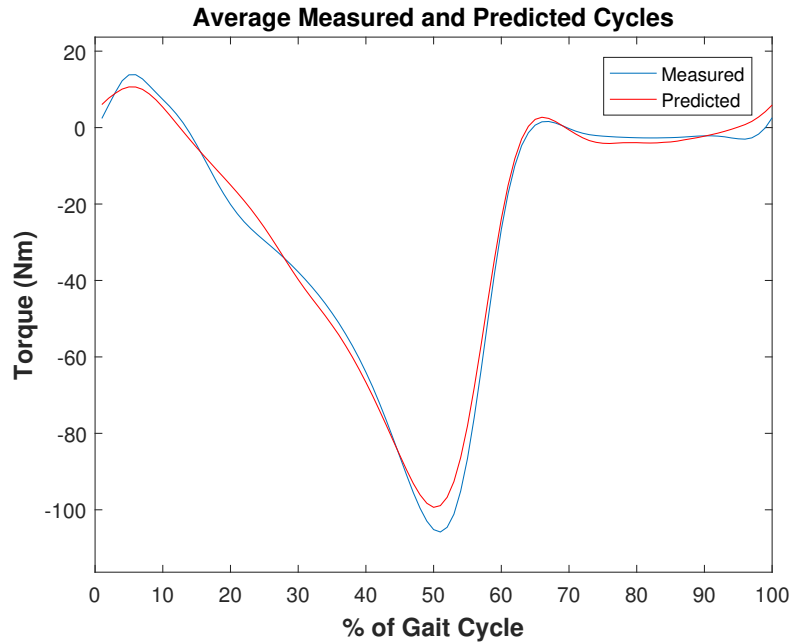


Figure 4.4: Measured (blue) and predicted (red) joint torque as a function of the gait cycle

The predicted and measured joint torques were compared at each point in every gait



cycle to determine how well the VMR system describes the particular point in the gait cycle. The linear regression line (red) at 60% of the gait cycle is shown in Figure 4.5, where the measured and predicted joint torques are plotted against each other. Note that each point represents one data point for each gait cycle, or every instance of 60% of the gait cycle throughout the entire trial. The slope of the regression line indicates that the VMR system adequately described this portion of the subject’s gait cycle.

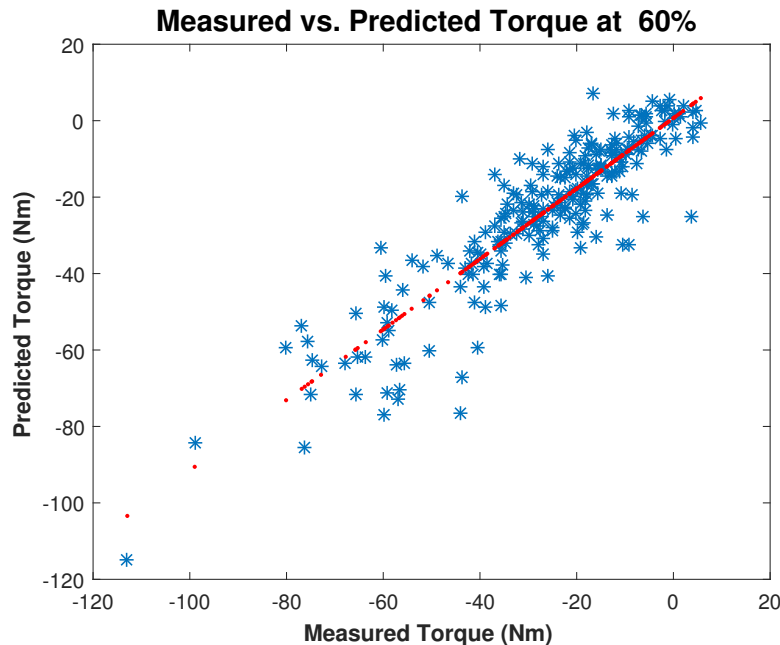


Figure 4.5: Correlation between measured and predicted joint ankle torque at 60% of the gait cycle. Note that each point represents one data point for every gait cycle, in this case  $N = 470$  gait cycles

Lastly, Figure 4.6 shows the correlation coefficients  $R^2$  for the entire gait cycle. Based on these preliminary results, the VMR system seems to perform best during the swing phase (60% and 90%), immediately after ankle push-off, and worst just before and after heelstrike (90% to 10%). However, this result is contingent on both the test subject and the speed of the trial. It is expected that control strategies may vary between individuals, or the same individual at slower or faster speeds. However, even  $R^2$  values of 0.5 are significant, given the large amount of gait cycles used in the simulation.

Initially, we believed the best correlation should occur at peak joint torque, where the majority of the deviations due to perturbations occur. However, based on current difficulties of reflex controllers in achieving accurate foot placement in hardware [23, 22], it may be more beneficial for the reflex controller to adequately place the foot at heelstrike rather than match the peak torque. It is expected these results will also change when the muscles of the upper leg are added to the VMR system, including their corresponding reflex control.

Additionally, it is possible for  $R^2$  to be negative, as indicated between 0-10% and 95-100% of the gait cycle (Figure 4.6), suggesting poor predictions during heelstrike. In this simulation study, it is impossible to conclude if the poor correlation before ankle push-off

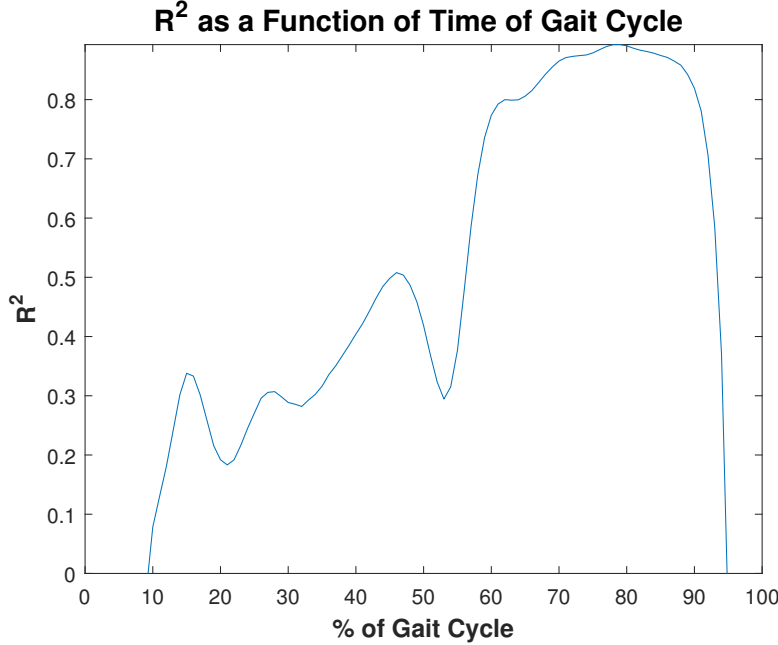


Figure 4.6: Coefficient of determination  $R^2$  as a function of time in the gait cycle. Each correlation coefficient was based on 470 gait cycles in this 8-minute recording

would produce noticeable consequences when tested in hardware.

An acceptable platform to investigate this more thoroughly would be a prosthetic device with an actuated ankle. However, this extends beyond the scope of this proposal as the ankle joint in the Indego exoskeleton is not actuated. When the VMR system is expanded to the knee and hip, the torque at the ankle joint can be reevaluated to check if these discrepancies persist with the addition of muscles in the upper leg. This will both provide insight and predict challenges for any future study involving the ankle VMR controller in hardware.

In the event the controller of Geyer and Herr still does not fit the data, the controller architecture can be modified by adding nonlinear terms with separate coefficients. Reflexes have been shown to respond to perturbations in simulation [22], though such controllers may not describe actual human data. Nonlinear terms may be required to replicate human responses, which may not be directly proportional to force feedback.

## 4.5 Status and Contribution

The optimizations and statistical analysis of all trials are only partially completed. Currently, the VMR system has been tested for the ankle joint, controlled by reflexes in the lower leg muscles (Soleus, Tibialis Anterior, and Gastrocnemius).

A more thorough analysis of the results will be conducted on the resulting joint torque of the ankle controller. Optimizations will be performed for all trials using all test subjects and speeds. Cross correlations between different portions of the same trial, different speeds with the same test subject, and between test subjects will demonstrate if the reflex controller is capable of describing a general control mechanism which can sufficiently replicate gait across

many individuals and speeds. For example, an optimized controller for one subject at one speed will predict the joint torques given the joint angle data of a different subject at a different speed.

After the preliminary evaluation of the ankle VMR controller, the model will be expanded to include the reflexes in the hip and the knee. Details of these relationships can be referenced in Appendix D.2. Adding these parameters will increase in complexity of the control, as well as the number of optimization parameters. The same optimization and statistical analysis techniques will be repeated with the inclusion of these additional joints.

Previously, neuromuscular reflex controllers had only been manually tuned until walking was achieved in simulation studies [22]. This is the first attempt using experimental data of perturbed walking to define the parameters of reflex controllers. Additionally, reflex controllers have yet to be evaluated through statistics to realize their potential. The preliminary statistical results suggest that reflexes can replicate many aspects of the human control strategy with high correlation throughout the majority of the gait cycle.

# Chapter 5

## Hardware Implementation

The VMR system must be implemented in hardware to assess if neuromuscular reflex controllers are practical in application and can produce natural gait mechanics. Suitable platforms are either a lower-limb prosthetic device or exoskeleton. However, neither virtual muscles or reflexes have been programmed in an exoskeleton, though they have demonstrated success in prosthetic devices such as the BiOM [21]. Recent improvements have been made to the swing leg reflex control and tested in the hardware of a transfemoral prosthesis, but design challenges prohibited a full implementation [23].

Controlling an exoskeleton avoids several difficulties that arise in the control of prosthetic devices. In particular, the user may alter their control strategy in response to the attachment of the prosthetic. The adjustments in gait mechanics may not correlate to the strategies of able-bodied subjects that were used to design the controller. Yet, in an exoskeleton, the user can only influence the movement by adjusting the position of their trunk.

Ideally, a subject wearing the exoskeleton would report improved performance and comfort using the reflex controller over the preexisting PD control [8]. The hardware implementation is separated into two phases: (1) observing the passive properties of muscles using isometric and isokinetic tests in a Biodex rehabilitation machine, described in Section 5.1, and (2) a demonstration of the full VMR system to actuate the electric motors at the hip and knee of the Indego, summarized in Section 5.2. Before testing in hardware, the preliminary simulation results of isometric and isokinetic test cases are shown in Section 5.3.

### 5.1 Ankle Virtual Muscles in the Indego Exoskeleton

The first hardware test involves programming the virtual muscles of the ankle (Soleus, Tibialis Anterior, and Gastrocnemius), without reflexes, into the Indego exoskeleton. Aforementioned, the Indego is actuated by electric motors at the knee and hip. However the knee joint can be programmed to behave as though it were an ankle without repercussions. The advantage of virtual muscle models is that the electric motors are subject to the muscles prescribed to it. Therefore, the knee joint can be used as an ankle and produce the appropriate forces and torques, despite its geometrical location.

To see if the virtual muscles programmed in the Indego can perform similarly to humans, a Biodex rehabilitation machine uses a dynamometer to restore strength to individuals suf-

fering from an injury. Standard isokinetic and isometric tests monitor the improvement of patients by comparing their output forces, joint velocities, and torques throughout their rehabilitation.

In place of a human test subject, the Indego will perform the standard isometric and isokinetic tests used in clinical applications. First, the joint torque measured by the Biodex and the joint torques prescribed by the virtual muscles will be compared, to observe if the hardware can execute the commanded torque. Secondly, the performance of the Indego can be compared to results in similar test conditions [27, 28, 29]. This literature suggests that ankle movements should range between  $10^\circ$  dorsiflexion (DF) and  $30^\circ$  plantarflexion (PF), with the knee joint held at  $45^\circ$  flexion.

The Indego will be tested in the following isometric tests conditions: 5 maximal contractions of DF (held at  $0^\circ$  PF), 5 maximal contractions of PF (held at  $25^\circ$  PF), and 5 sinusoidal activations (0 to 1 muscle activation, 1 Hz frequency). Isokinetic tests include DF and PF at 30 and  $90^\circ/\text{s}$ , as well as an extremely slow trial in both DF and PF.

Before testing on the Indego, it must be proven that the VMR system of the ankle responds appropriately given the test conditions of the Biodex. Therefore, the following tests were performed in simulation:

- **Isometric Simulations.** The joint angles of the hip, knee, and ankle were set to  $0^\circ$ ,  $45^\circ$ , and  $0^\circ$ , respectively. First, both PFs were activated from 0 to 1 to observe the corresponding torque in the ankle, while the DFs were held at 0 activation. Then, the DFs were activated and the PFs deactivated. The test was repeated on different orientations of the ankle joint, simulating the standard isometric tests which would be performed on a Biodex.
- **Isokinetic Simulations.** Similarly, the joint angles of the hip and knee were set to  $0^\circ$  and  $45^\circ$ . However, the ankle angle was controlled by a sawtooth wave, set to the range of  $10^\circ$  DF and  $30^\circ$  PF with a frequency of 1 Hz. This simulated a standard isokinetic test which would be performed on the Biodex.

The results of these simulated test cases are summarized in Section 5.3. After the ankle VMR system behaves appropriately given the isometric and isokinetic tests, it will then be tested on the Biodex.

## 5.2 Hip and Knee VMR Control in Indego Exoskeleton

Similar to the ankle VMR control, the MATLAB Simulink of the Indego will be updated to include the hip and knee, with reflex parameters optimized from the perturbed walking data. However, though the VMR system is capable of being implemented in the hardware, the results are not immediately clear. For instance, a reflex controller for the hip has never been tested in hardware, nor in an exoskeleton where postural stability is crucial.

Additional information, including the trunk lean angle for maintaining postural stability, as well as knowledge of the forces in the contralateral and ipsilateral leg, will introduce challenges in hardware implementation. Though the Indego has a trunk position sensor, force sensing resistors will be added underneath the foot supports of the exoskeleton, measured

in real-time within the same MATLAB Simulink which controls the electric motors. Lastly, though the ankle is not actuated in the Indego, an encoder will be added to the joint in order to properly simulate the biarticular Gastrocnemius, which crosses between the knee and ankle joints. The position of the ankle will influence the torque contribution of the Gastrocnemius on the knee, even though the ankle itself is not being actively controlled.

Therefore, testing the full VMR system in the Indego will be for demonstration purposes only. A pilot study will involve one subject wearing the exoskeleton and walking on the treadmill, first using both the predefined PD controller. This PD controller uses phase-based switching between the single support, double support, and swing phases of gait, resulting in stagnated movements [8]. Then, the subject will walk with the new VMR system. Ideally, the subject will report a more comfortable and natural gait. However, extensive testing of the controllers, namely a quantitative comparison of PD, impedance, and reflex controllers, extends beyond the scope of this proposal.

### 5.3 Results

The ankle VMR system responds accordingly to the prescribed motions. Figure 5.1 illustrates the results of holding the joint angles of the hip, knee, and ankle, constant at  $0^\circ$ ,  $45^\circ$ , and  $0^\circ$ , respectively. First, the PFs were fully activated from 0 to 1 and the corresponding joint torque was observed (left). Then, the DFs were activated when the PFs were deactivated (right).

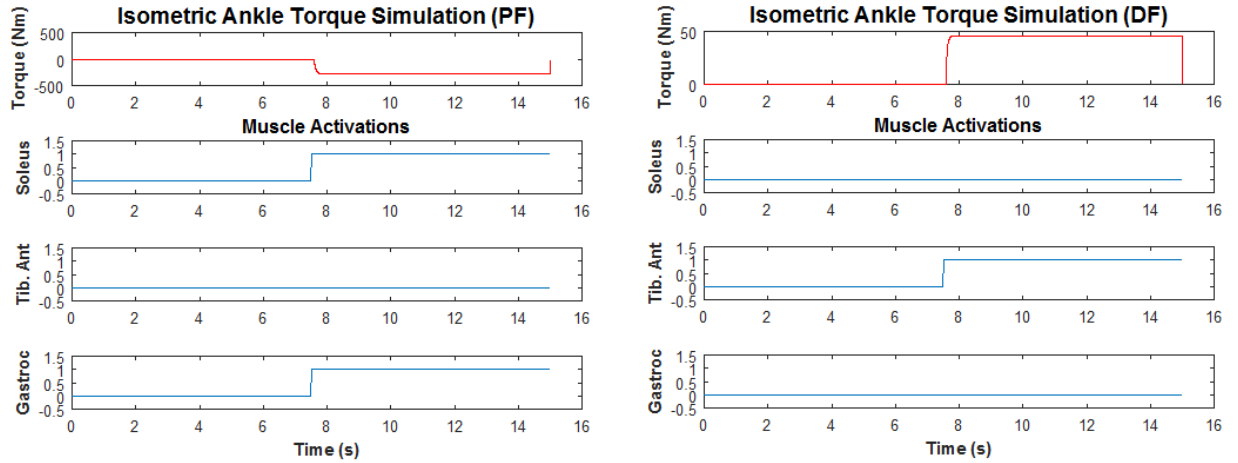


Figure 5.1: Ankle joint torque (top) of the isometric simulation tests with the plantarflexor (PF) muscles fully activated (left) and dorsiflexor (DF) muscles fully activated (right)

Activating either the PFs or the DFs produce a torque in the appropriate direction. With an ankle position of  $0^\circ$ , the PFs are capable of producing more torque, as indicated on the graph, as opposed to the DFs. This is because the length of DF muscle (Tibialis Anterior) is very short in this position and can only produce minimal force. In the condition of maximal PF, the DFs will produce more torque than the PFs for the same reason. Therefore, it is appropriate to assume the VMR system will react reasonably in the isometric test condition.

Similarly, the results of the isokinetic simulations are shown in Figure 5.2. Here, the hip and knee were held at  $0^\circ$  and  $45^\circ$ , while the ankle angle was moved between a maximum PF of  $30^\circ$  and DF of  $10^\circ$  using a sawtooth wave with a 1 Hz frequency. The plantarflexors were first activated (left) and then the dorsiflexors (right) to simulate the isokinetic tests conditions of the Biodex.

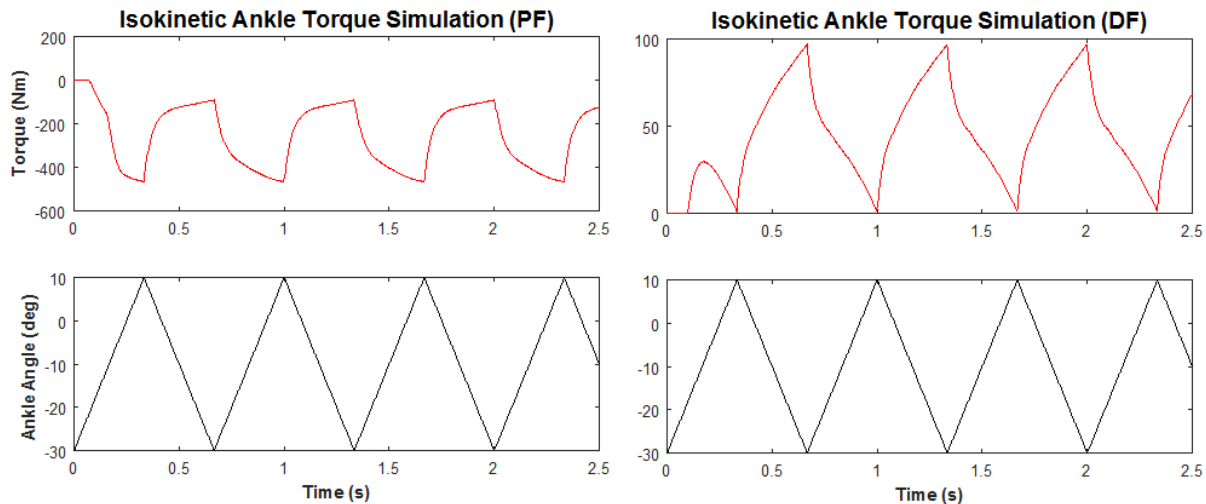


Figure 5.2: Ankle joint torque (top) of the isokinetic simulation tests with the PF muscles fully activated (left) and the DF muscles fully activated (right) when the ankle angle was moved in a sawtooth trajectory (bottom)

The joint torque corresponds to the motion of the ankle, depending on if the DFs or PFs are activated. In each case, the torque is in the appropriate direction. When the ankle is moved to maximum DF, the PFs produce more torque. Alternatively, when the ankle is moved to maximum PF, the DFs produce more torque.

The behavior of the isokinetic and isometric simulations indicate that the ankle VMR system will respond accordingly to the test conditions performed by the Biodex.

## 5.4 Status and Contribution

The majority of the hardware tests are still in progress. Currently, the virtual muscles of the ankle have been successfully programmed in the Indego, in place of the current PD controller. Pilot tests were performed at the Cleveland Clinic in Cleveland, Ohio, shown in Figure 5.3. In the upcoming studies, a Biodex-II machine at Cleveland State University will be used to record the joint torques for all test conditions.

After evaluating the performance of the ankle, the model will then be expanded to include the hip and the knee. The demonstration test comparing the preexisting PD controller on the Indego and the new VMR system will be qualitatively compared.

Aforementioned, a neuromuscular reflex controller has never been implemented in an exoskeleton. Though success is reported in prosthetic devices [21, 23], the reflex control for



Figure 5.3: Indego Exoskeleton on a Biodex rehabilitation machine at the Cleveland Clinic. The Indego is programmed with virtual muscles of the Soleus, Tibialis Anterior, and Gastrocnemius, where the knee joint behaves as though it were an ankle

the hip has never been tested in hardware. This research will show if the VMR system can produce locomotion and maintain postural stability in actual hardware.



## Chapter 6

# Timeline for Remaining Research Objectives

This section briefly outlines the timeline and implementation strategy for the remaining objectives, illustrated in Figure 6.1. Throughout the remaining objectives, a more thorough literature review will detail: (1) current prosthetic devices, including both passive and active control strategies, (2) current exoskeletons and an explanation of their control, and (3) currently proposed neurologically-inspired controllers.

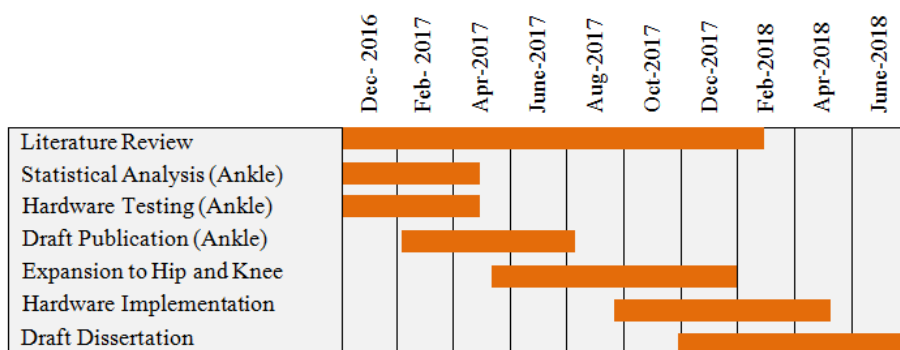


Figure 6.1: Projected timeline for completing outstanding research objectives

First, the optimization, statistical analysis, and hardware testing of the ankle VMR system will be conducted. We intend to publish the results of this portion of the research. Then, all optimizations and statistics will be repeated for the VMR system after expanding the controller to the hip and knee. Lastly, the optimized system will be programmed into the Indego exoskeleton for demonstration purposes.

# Appendix A

## Motion Capture Marker Set

A standard, full-body marker set consisting of 47 markers was used in the perturbation experiments [39]. Markers are placed both on anatomically relevant features, while others ensure the motion capture system can properly distinguish between the left and right sides of the body. A description of the marker set is shown in Figures A.1 and A.2.

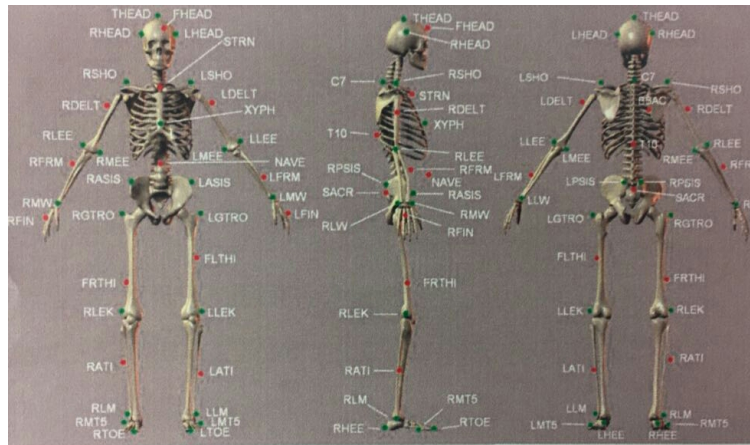


Figure A.1: Full-body marker set consisting of 47 markers used in the perturbation experiments

#	Label	Name	#	Label	Name
1	LHEAD	Left Head	28	LASIS	Pelvic bone left front
2	THEAD	Top Head	29	RASIS	Pelvic bone right front
3	RHEAD	Right Head	30	LPSIS	Pelvic bone left back
4	FHEAD	Forehead	31	RPSIS	Pelvic bone right back
5	C7	7th cervical spine	32	LGTRO	Left greater trochanter of the femur
6	T10	10th thoracic spine	33	FLTHI	Left thigh
7	SACR	Sacrum bone	34	LLEK	Left lateral epicondyle of the knee
8	NAVE	Navel	35	LATI	Left anterior of the tibia
9	XYPH	Xiphoid process	36	LLM	Left lateral malleolus of the ankle
10	STRN	Sternum	37	LHEE	Left heel
11	BBAC	Scapula	38	LTOE	Left toe
12	LSHO	Left shoulder	39	LMT5	Left 5th metatarsal
13	LDELT	Left deltoid muscle	40	RGTRO	Right greater trochanter of the femur
14	LLEE	Left lateral elbow	41	FRTHI	Right thigh
15	LMEE	Left medial elbow	42	RLEK	Right lateral epicondyle of the knee
16	LFRM	Left forearm	43	RATI	Right anterior of the tibia
17	LMW	Left medial wrist	44	RLM	Right lateral malleolus of the ankle
18	LLW	Left lateral wrist	45	RHEE	Right heel
19	LFIN	Left fingers	46	RTOE	Right toe
20	RSHO	Right shoulder	47	RMt5	Right 5th metatarsal
21	RDELT	Right deltoid			
22	RLEE	Right lateral elbow			
23	RMEE	Right medial elbow			
24	RFRM	Right forearm			
25	RMW	Right medial wrist			
26	RLW	Right lateral wrist			
27	RFIN	Right fingers			

Figure A.2: Detailed locations of the 47 markers used in the marker set

# Appendix B

## Musculotendon Model

Muscle activation (3.1) and contraction (3.2) dynamics of Section 3 are calculated using the isometric force-length relationship at maximum activation ( $F_1$ ), the force-velocity relationship ( $F_2$ ), the force contribution of the series and parallel elastic elements ( $F_{SEE}$ ,  $F_{PEE}$ ) and small viscous damping of the contractile element ( $F_{damp}$ ). For faster computation time, all calculations are normalized to the maximum isometric muscle force,  $F_{max}$  and optimal length of the contractile element,  $L_{CE,opt}$ .

The contribution of the force-length relationship is calculated in (B.1), where  $W$  is the width of the contractile element's force-width relationship and  $L_{CE}$  is the length of the contractile element:

$$F_1 = \exp\left(\frac{L_{CE} - 1}{W}\right)^2 \quad (\text{B.1})$$

The contribution of the force-velocity relationship is dependent on the direction of velocity. If the velocity of the contractile element ( $\dot{L}_{CE}$ ) is decreasing, then the muscle experiences concentric contraction:

$$F_2 = \frac{V_{max} + \dot{L}_{CE}}{V_{max} - A} \quad (\text{B.2})$$

where  $V_{max}$  is the maximum contraction velocity of the muscle and  $A$  is a constant variable of 0.25 used in Hill-muscle models.

However, if the velocity is increasing, then the muscle undergoes eccentric contraction:

$$F_2 = \frac{G_{max} + c}{\dot{L}_{CE} + c} \quad (\text{B.3})$$

where  $G_{max}$  is the maximum eccentric force of the muscle, and  $c$  is a continuity parameter for eccentric force-velocity relationship.

In Hill-muscle models, both the series and parallel elastic elements are modeled as non-linear springs, where force cannot be produced until the slack-length of the element is superseded. However, after the length of the element is greater than the slack-length, the force contribution becomes a quadratic relationship of the difference between the current length and slack-length. Therefore,  $F_{PEE}$  and  $F_{SEE}$  are represented by two sets of equations, depending on positive or negative deformations.

If the elongation of the PEE is positive, then the  $F_{PEE}$  can be calculated by multiplying the stiffness  $k_{PEE}$  by the squared difference in  $L_{CE}$  and the slack-length of the PEE,  $PEE_{slack}$ :

$$F_{PEE} = k_{PEE} (L_{CE} - PEE_{slack})^2 \quad (\text{B.4})$$

Similarly, force in the  $F_{SEE}$  can be calculated by multiplying the stiffness  $k_{SEE}$  and the squared length of  $SEE$ , which is the length of the muscle  $L_m$  subtracted by  $L_{CE}$  and the slack-length of the SEE:

$$F_{SEE} = k_{SEE} (L_m - L_{CE} L_{CE,opt} - SEE_{slack})^2 \quad (\text{B.5})$$

Ultimately, the force in the  $SEE$  determines the force of the muscle. This force,  $F_{SEE}$  will then be multiplied by the moment arm,  $d$ , to determine the torque contribution of that muscle,  $i$ , on their respective joints:

$$\tau_{joint} = \sum_i d_{joint,i} F_{SEE,i} \quad (\text{B.6})$$

However, numerical stability occurs when the the derivative of the muscle force with respect to  $\dot{L}_{CE}$  is zero. To prevent this, a small amount of viscous damping ( $F_{damp}$ ) is added in parallel to the contractile element. It is reasonable to assume this damping is indeed a physical property of muscles, considering the high water content of muscle tissue [66, 44, 67]. This damping force is calculated by multiplying a damping coefficient,  $\beta$ , by  $\dot{L}_{CE}$ .

A description of all muscle parameters used is shown in Table B.1. The nominal properties of these muscles were obtained from previous literature [54].

Table B.1: Muscle parameters used in the three-element Hill-model which describe muscle contraction and activation dynamics

<b>Parameter</b>	<b>Description</b>
$F_{max}$	Maximal isometric force of $CE$ (N)
$L_{ce,opt}$	Optimal length of $CE$ (m)
$Width$	Width of $CE$ force-length relationship (m)
$PEE_{slack}$	Slack-length of the $PEE$ , relative to $L_{ce,opt}$
$SEE_{slack}$	Slack length of the $SEE$ (m)
$L_0$	Muscle-tendon length when all DOFs are zero
$d_{hip}$	hip moment arm
$d_{knee}$	knee moment arm
$d_{ankle}$	ankle moment
$k_{PEE}$	Stiffness parameter of $PEE$ , in $F_{max}/L_{ce,opt}^2$
$u_{max}$	strain of $SEE$ at $F_{max}$ load
$V_{max}$	Maximum contraction velocity in $L_{ce,opt}/s$
$T_{act}$	activation time constant
$T_{deact}$	deactivation time constant
$g_{max}$	maximum eccentric force
$A$	Hill's a parameter, relative to $F_{max}$
$delay$	delay for the muscle's sensory feedback from reflexes

# Appendix C

## First-order Rosenbrock Solver for Muscle Dynamics

For use in hardware, the muscle model must perform all calculations at least as fast as real-time. A fixed-step, implicit formulation of musculoskeletal dynamics has been developed [26] which can produce accurate results in real-time.

Using this method, the muscle activation (3.1) and contraction (3.2) relationships (Section 3) can be combined into a single, implicit state equation:

$$f(x, \dot{x}, u) = 0 \quad (\text{C.1})$$

with state variables  $x_n = [L_{CE} \ a]^T$  and state derivatives  $\dot{x}_n = [\dot{L}_{CE} \ \dot{a}]^T$ , where  $L_{CE}$  is the length of the contractile element and  $a$  is the muscle activation signal. The control inputs,  $u$ , are the neural excitation control signals generated by the reflex controller (Section 4, Appendix D). This implicit formulation of forward muscle dynamics can be solved using a fixed-step, linear, first-order Rosenbrock implicit differential equation solver:

$$\left( \left( \frac{\partial f}{\partial x} \right) + \frac{1}{h} \frac{\partial f}{\partial \dot{x}} \right) \Delta x = \left( \frac{\partial f}{\partial \dot{x}} \dot{x}_n - f(x_n, \dot{x}_n, u_n) \right) - \frac{\partial f}{\partial u} (u_{n+1} - u_n) \quad (\text{C.2})$$

In the state equations for muscle dynamics, we have state variables  $x_n = [L_{CE} \ a]^T$  and state derivatives  $\dot{x}_n = [\dot{L}_{CE} \ \dot{a}]^T$ , where  $n$  is the number of samples,  $L_{CE}$  is the length of the contractile element,  $a$  is the muscle activation signal,  $u$  is the neural excitation signal, and  $h$  is the step-size of the solver.

Based on the muscle dynamics equations, the relationships of C.2 can be defined as

follows:

$$\frac{\partial f}{\partial x} = \begin{bmatrix} \frac{\partial f_1}{\partial L_{CE}} & \frac{\partial f_1}{\partial a} \\ 0 & \frac{\partial f_2}{\partial a} \end{bmatrix} \quad (\text{C.3a})$$

$$\frac{\partial f}{\partial \dot{x}} = \begin{bmatrix} \frac{\partial f_1}{\partial \dot{L}_{CE}} & 0 \\ 0 & \frac{\partial f_2}{\partial \dot{a}} \end{bmatrix} \quad (\text{C.3b})$$

$$\frac{\partial f}{\partial u} = \begin{bmatrix} 0 & \frac{\partial f_2}{\partial u} \end{bmatrix}^T \quad (\text{C.3c})$$

For brevity, the partial-derivatives of each force contribution required by the Rosenbrock solver have been omitted. In order to be used in low-level programming languages, the Rosenbrock solver can be reformulated C.2 as a system of linear equations:

$$\begin{bmatrix} A & B \\ C & D \end{bmatrix} = \Delta x \begin{bmatrix} E \\ F \end{bmatrix}$$

Substituting the relationships C.3a - C.3c into the linear form, we obtain:

$$\begin{aligned} A &= \frac{\partial f_1}{\partial L_{CE}} + \frac{1}{h} \frac{\partial f_1}{\partial \dot{L}_{CE}} & D &= \frac{\partial f_2}{\partial a} + \frac{1}{h} \frac{\partial f_2}{\partial \dot{a}} \\ B &= \frac{\partial f_1}{\partial a} & E &= \frac{\partial f_1}{\partial \dot{L}_{CE}} \dot{L}_{CE} - f_{cont} \\ C &= 0 & F &= \frac{\partial f_2}{\partial \dot{a}} \dot{a} - f_{act} - \frac{\partial f_2}{\partial u} (u_{n+1} - u_n) \end{aligned}$$

where  $f_{cont}$  and  $f_{act}$  represent muscle contraction and muscle activation, respectively. Therefore, the change in state between each time-step can be simulated by a set of independent linear equations:  $\Delta x_{LCE} = (E - B\Delta x_a)$  and  $\Delta x_a = F/D$ . This formulation allows for muscle simulations well within the range of real-time requirements.



# Appendix D

## Reflex Model

The reflex controller described by Geyer and Herr [20] is summarized here. Section D.1 outlines the reflexes exhibited by the muscles of the ankle (Soleus, Tibialis Anterior (TA), and Gastrocnemius). Additionally, Section D.2 details the reflex equations for the muscles in the upper leg, including the Vasti, Hamstrings, Gluteus, and hip flexors (HFL), which will be implemented in future work.

### D.1 Ankle Reflexes

The equations describing reflexes in the ankle muscle groups (Soleus, Tibialis Anterior, and Gastrocnemius) are simple relationships involving the muscle pre-stimulations  $S_m$ , gained force,  $G_m F_m$ , and neural delays,  $t_m$ .

However, the monoarticular Tibialis Anterior (TA) is modeled using both positive force and length feedback to prevent the ankle from hyperextending when the knee produces large torques. This can occur because the Gastrocnemius is a biarticular muscle which crosses both the knee and ankle, thereby influencing the movement in both joints. The positive length feedback terms in the TA are length of the contractile element in the TA ( $L_{CE}$ ) and the length offset of attachment from the ankle  $l_{OFF,TA}$ . Additionally, a negative force feedback from the Soleus muscle ( $G_{SOLTA}$ ) prevents the TA from constantly resisting the Gastrocnemius. The stance reflex equations for are shown in Equations D.1 - D.3, below.

$$u_{SOL} = S_{0,SOL} + G_{SOL} F_{SOL} (t - t_{SOL}) \quad (D.1)$$

$$u_{TA} = S_{0,TA} + G_{TA} [(L_{CE}(t_{TA}) - l_{OFF,TA})] G_{SOLTA} F_{SOL} (t - t_{TA}) \quad (D.2)$$

$$u_{GAS} = S_{0,GAS} + G_{GAS} F_{GAS} (t - t_{GAS}) \quad (D.3)$$

During the swing phase, the reflexes in the Soleus and Gastrocnemius are simply the pre-stimulation:  $u_{SOL} = S_{0,SOL}$  and  $u_{GAS} = S_{0,GAS}$ . In the case of the TA, the negative force feedback from the Gastrocnemius is no longer included:

$$u_{TA} = S_{0,TA} + G_{TA} [(L_{CE}(t_{TA}) - l_{OFF,TA})] \quad (D.4)$$

Therefore, there are 8 control parameters included in the optimization described in Section 4.2: the pre-stimulations and gains of the 3 muscles, as well as the negative force feedback gains ( $G_{SOLTA}$ ) and length offset ( $l_{OFF,TA}$ ) in the TA.

## D.2 Knee and Hip Reflexes

The following relationships which govern the movement of the knee and hip will be added to the VMR system, for testing in both simulation and hardware. These equations require additional sensory information, particularly the lean angle of the trunk.

During the swing phase, the Vasti muscle group can be described as the muscle pre-stimulation only:  $u_{VAS} = S_{0,VAS}$ . However, during the stance phase, knee hyperextension is prohibited by adding an angle threshold  $\varphi_k$ . Also, positive force feedback is inhibited by the force in the contralateral leg, ( $F_{ipsi}$ ), in which a gain parameter  $k_{bw}$  determines the degree of inhibition. This term is regulated by  $D_{Sup}$ , which varies between 0 and 1 depending on if the leg is in single or double support phase, respectively:

$$u_{VAS} = S_{0,VAS} + G_{VAS}F_{VAS}(t_{VAS}) - k_{\varphi}[\varphi(t_{VAS}) - \varphi_{k,off}][\varphi_k(t_{VAS}) > \varphi_{k,off} \quad (\dot{\varphi}_k(t_{VAS}) > 0] - k_{bw}|F_{contra}(t_{VAS})|D_{Sup} \quad (D.5)$$

Positive force feedback in the Hamstrings (D.6) and Gluteus (D.7) guarantee that the leg continues to produce forward momentum instead of locking in place:

$$u_{HAM} = S_{0,HAM} + G_{HAM}F_{HAM}(t - t_{HAM}) \quad (D.6)$$

$$u_{GLU} = S_{0,GLU} + G_{GLU}F_{GLU}(t - t_{GLU}) \quad (D.7)$$

Postural stability in the trunk during the stance phase is maintained by adding a PD control to the Hamstrings, Gluteus, and hip flexors. PD control corrects the difference between the current trunk lean angle,  $\theta$ , and trunk's pitch at toe-off,  $\theta_{off}$ . The muscles of the hip are also influenced when the Vasti muscles respond to the force in the contralateral leg. This ipsilateral force ( $F_{ipsa}$ ) stimulates the force feedback in the hip flexors (D.8) while inhibiting the force feedback in the Gluteus (D.9) during double support:

$$u_{HFL} = S_{0,HFL} + \{k_{p,GLU}[\theta(t_{HFL}) - \theta_{ref}] + k_d\dot{\theta}(t_{HFL})\} - k_{bw}|F_{ipsi}(t_{HFL})| + \Delta SD_{Sup} \quad (D.8)$$

$$u_{GLU} = S_{0,GLU} + \{k_{p,GLU}[\theta(t_{GLU}) - \theta_{ref}] + k_d\dot{\theta}(t_{GLU})\} + k_{bw}|F_{ipsi}(t_{HAM})| - \Delta SD_{Sup} \quad (D.9)$$

The force in the ipsilateral leg also inhibits the positive force feedback of the Hamstrings:

$$u_{HAM} = S_{0,HAM} + \{k_{p,HAM}[\theta(t_{HAM}) - \theta_{ref}] + k_d\dot{\theta}(t_{HAM})\} + k_{bw}|F_{ipsi}(t_{HAM})| \quad (D.10)$$

In the swing phase, the hip flexors are innervated by positive length feedback, dictated by the length of the contracile element,  $L_{CE}$ , and the offset distance between the hip flexor and hip joint,  $l_{OFF,HFL}$ . Feedback from the Hamstrings,  $G_{HAMHFL}$ , regulates the retraction of the hip, which ensures proper foot placement at heelstrike.

$$u_{HFL} = S_{0,HFL} + G_{HFL}[(L_{CE}(t_{HFL}) - l_{OFF,HFL})] - G_{HAMHFL}[(L_{CE}(t_{HAM}) - l_{OFF,HAM})]\{[\theta(t_{HFL}) - \theta_{ref}]\} \quad (\text{D.11})$$

# Bibliography

- [1] E. R. Kandel, J. H. Schwartz, T. M. Jessel, and S. A. Siegelbaum. *Principles of Neural Science*. McGraw-Hill, New York, 2000.
- [2] J. Nolte. *The Human Brain: An Introduction to its Functional Anatomy*. Springer-Verlag, New York, 1988.
- [3] L. J. Marks and J. W. Michael. Artificial limbs. *BMJ: British Medical Journal*, 323(7315):732–735, 2001.
- [4] C. Horne and J. Neil. Quality of life in patients with prosthetic legs: A comparison study. *Journal of Prosthetics and Orthotics*, 21(3):154–159, 2009.
- [5] D. A. Winter. *Biomechanics and motor control of human movement*. J. Wiley and Sons, New York, 1990.
- [6] F. Sup, A. Bohara, and M. Goldfarb. Design and control of a powered transfemoral prosthesis. *International Journal of Robotics Research*, 27(2):263–273, 2008.
- [7] B. E. Lawson, B. Ruhe, A. Shultz, , and M. Goldfarb. A powered prosthetic intervention for bilateral transfemoral amputees. *IEEE Transactions on Biomedical Engineering*, 62(4):1042–1050, 2015.
- [8] R. J. Farris, H. A. Quintero, S. A. Murray, , K. H. Ha, C. Hartigan, and M. Goldfarb. A preliminary assessment of legged mobility provided by a lower limb exoskeleton for persons with paraplegia. *IEEE Transactions on Neural Systems and Rehabilitation Engineering*, 22(3):482–490, 2014.
- [9] K. G. Gerritsen, A. J. van den Bogert, M. Hulliger, and R. F. Nernicke. Intrinsic muscle properties facilitate locomotor control - a computer simulation study. *Motor Control*, 2(3):206–220, 1998.
- [10] A. J. Ijspeert. Central pattern generators for locomotion control in animals and robots: A review. *Neural Networks*, 21(4):642–653, May 2008.
- [11] J. Yu, M. Tan, J. Chen, and J. Zhang. A survey on cpg-inspired control models and system implementation. *IEEE Transactions on Neural Networks and Learning Systems*, 25(3):441–456, March 2014.

- [12] A. Hodgkin and A. Huxley. A quantitative description of membrane current and its application to conduction and excitation in a nerve. *Journal of Physiology*, 117(4):500–544, August 1952.
- [13] P.J Whelan. Control of locomotion in the decerebrate cat. *Progress in Neurobiology*, 49(5):481–515, 1996.
- [14] N. Wenger, E. M. Moraud, S. Raspopovic, M. Bonizzato, J. DiGiovanna, P. Musienko, M. Morari, S. Micerea, and G. Courtine. Closed-loop neuromodulation of spinal sensorimotor circuits controls refined locomotion after complete spinal cord injury. *Science Translational Medicine*, 6(255), 2014.
- [15] K. Matsuoka. Sustained oscillations generated by mutually inhibiting neurons with adaption. *Biological Cybernetics*, 52(6):367–376, October 1985.
- [16] G. Taga. A model of the neuro-musculo-skeletal system for human locomotion. *Biological Cybernetics*, 73(2):113–121, July 1995.
- [17] I. Righetti, J. Buchli, and A. J. Ijspeert. Dynamic hebbian learning in adaptive frequency oscillators. *Physica D: Nonlinear Phenomenon*, 216(2):269–281, 2006.
- [18] J. E. Marsden and M. McCracken. *The Hopf Bifurcation and Its Applications*. Springer-Verlag, New York, 1976.
- [19] A. Crespi, K. Karakasiliotis, A. Guignard, and A. J. Ijspeert. Salamandra robotica ii: an amphibious robot to study salamander-like swimming and walking gaits. *IEEE Transactions on Robotics*, 29(2):308–320, 2013.
- [20] H. Geyer and H. Herr. A muscle-reflex model that encodes principles of legged mechanics produces human walking dynamics and muscle activities. *IEEE Transactions on Neural Systems and Rehabilitation Engineering*, 18(3):263–273, June 2010.
- [21] M. F. Eilenberg, H. Geyer, and H. Herr. Control of a powered ankle-foot prosthesis based on a neuromuscular model. *IEEE Transactions on Neural Systems and Rehabilitation Engineering*, 18(2):164–173, April 2010.
- [22] S. Song and H. Geyer. A neural circuitry that emphasizes spinal feedback generates diverse behaviours of human locomotion. *The Journal of Physiology*, 593(16):3493–3511, 2015.
- [23] N. Thatte and H. Geyer. Toward balance recovery with leg prostheses using neuromuscular model control. *IEEE Transactions on Biomedical Engineering*, 63(4):904–913, 2016.
- [24] F. Sup, H. A. Varol, and M. Goldfarb. Upslope walking with a powered knee and ankle prosthesis: Initial results with an amputee subject. *IEEE Transactions on Neural Systems and Rehabilitation Engineering*, 19(1):71–78, 2011.

- [25] B. E. Lawson, H. Atakan Varol, F. Sup, and M. Goldfarb. Stumble detection and classification for an intelligent transfemoral prosthesis. In *2010 Annual International Conference of the IEEE Engineering in Medicine and Biology*, pages 511–514, 2010.
- [26] A. J. van den Bogert, D. Blana, and D. Heinrich. Implicit methods for efficient musculoskeletal simulation and optimal control. *Procedia IUTAM*, 2:297–316, January 2011.
- [27] S. C. Webber and M. M. Porter. Reliability of ankle isometric, isotonic, and isokinetic strength and power testing in older women. *Physical Therapy*, 90(8):1165–1175, 2010.
- [28] A. M. Moseley, J. Crosbie, and R. Adams. Normative data for passive ankle plantarflexion–dorsiflexion flexibility. *Clinical Biomechanics*, 16(6):514–521, 2001.
- [29] H. Karnofel, K. Wilkinson, and G. Lentell. Reliability of isokinetic muscle testing at the ankle. *Journal of Orthopaedic & Sports Physical Therapy*, 11(4):150–154, 1989.
- [30] J. K. Moore, S. K. Hnat, and A. J. van den Bogert. An elaborate data set on human gait and the effect of mechanical perturbations. *PeerJ PrePrints*, 3:e1248, 4 2015.
- [31] J.K. Moore S.K. Hnat and A.J. van den Bogert. Perturbed data paper. *GitHub Repository*, 2014. Available at <https://github.com/csu-hmc/perturbed-data-paper>, version 1.0.
- [32] S. Park, F. B. Horak, and A. D. Kuo. Postural feedback responses scale with biomechanical constraints in human standing. *Experimental Brain Research*, 154(4):417–427, 2004.
- [33] C L. Chen, S Z. Lou, H W. Wu, S K. Wu, K T. Yeung, and F C. Su. Effects of the type and direction of support surface perturbation on postural responses. *Journal of Neuroengineering and Rehabilitation*, 1:50, 2014.
- [34] G. Pagnacco, A. Silva, E. Oggero, and N. Berme. Inertially compensated force plate: a means for quantifying subject’s ground reaction forces in non-inertial conditions. *Biomedical Sciences Instrumentation*, pages 397–402, 2000.
- [35] T. M. Owings, M. J. Pavol, and M. D. Grabiner. Mechanisms of failed recovery following postural perturbations on a motorized treadmill mimic those associated with an actual forward trip. *Clinical Biomechanics*, 16(9):813–819, 2001.
- [36] P. H. Sessoms, M. Wyatt, M. Grabiner, J-D. Collins, T. Kingsbury, N. Thesing, and K. Kaufman. Method for evoking a trip-like response using a treadmill-based perturbation during locomotion. *Journal of Biomechanics*, 47(1):277–280, 2014.
- [37] L H. Sloom, M. M. van der Krogt, and J. Harlaar. Effects of adding a virtual reality environment to different modes of treadmill walking. *Gait and Posture*, 39(3):939–945, 2014.
- [38] S. K. Hnat and A. J. van den Bogert. Inertial compensation for belt acceleration in an instrumented treadmill. *Journal of Biomechanics*, 47(15):3758 – 3761, 2014.

- [39] A. J. van den Bogert, T. Geijtenbeek, O. Even-Zohar, F. Steenbrink, and E. C. Hardin. A real-time system for biomechanical analysis of human movement and muscle function. *Medical and Biological Engineering and Computing*, 154:1069–1077, 2013.
- [40] S.K. Hnat, J.K. Moore, and A.J. van den Bogert. Pitch moment compensation. *GitHub Repository*, 2014. Available at <https://github.com/csu-hmc/pitch-moment-compensation>, version 1.0.
- [41] E. Eisenberg, T.L. Hill, and Y. Chen. Cross-bridge model of muscle contraction. quantitative analysis. *Biophysical Journal*, 29(2):195 – 227, 1980.
- [42] G. I. Zahalak and S. Ma. Muscle activation and contraction: Constitutive relations based directly on cross-bridge kinetics. *ASME Journal of Biomechanical Engineering*, 112:52–62, 1990.
- [43] J.C. Haselgrove and H.E. Huxley. X-ray evidence for radial cross-bridge movement and for the sliding filament model in actively contracting skeletal muscle. *Journal of Molecular Biology*, 77(4):549 – 568, 1973.
- [44] M. Millard, T. Uchida, A. Seth, and S.L. Delp. Flexing computational muscle: Modeling and simulation of musculotendon dynamics. *ASME Journal of Biomechanical Engineering*, 135(2):0210051–02100511, 2013.
- [45] S. X. Sun, S. Walcott, and C. W. Wolgemuth. Cytoskeletal cross-linking and bundling in motor-independent contraction. *Current Biology*, 20(15):R649 – R654, 2010.
- [46] S. Walcott and W. Herzog. Modeling residual force enhancement with generic cross-bridge models. *Mathematical Biosciences*, 216(2):172 – 186, 2008.
- [47] S. Walcott and S. X. Sun. A mechanical model of actin stress fiber formation and substrate elasticity sensing in adherent cells. *Proceedings of the National Academy of Sciences*, 107(17):7757–7762, 2010.
- [48] F. E. Zajac. Muscle and tendon: properties, models, scaling, and application to biomechanics and motor control. *Critical Reviews in Biomedical Engineering*, 17(4):359–411, 1989.
- [49] J M Winters and L Stark. Muscle models: What is gained and what is lost by varying model complexity. *Biological Cybernetics*, 55(6):403–420, 1987.
- [50] J. M. Winters and S. L-Y. Woo. *Multiple Muscle Systems: Biomechanics and Movement Organization*. Springer-Verlag, New York, 1990.
- [51] A. V. Hill. The heat of shortening and the dynamic constants of muscle. *Proceedings of the Royal Society of London B: Biological Sciences*, 126(843):136–195, 1938.
- [52] M. Roche. Rosenbrock methods for differential algebraic equations. *Numerische Mathematik*, 52(1):45–63, 1987.

- [53] H. H. Rosenbrock. Some general implicit processes for the numerical solution of differential equations. *The Computer Journal*, 5(4):329–330, 1963.
- [54] K. G. M. Gerritsen, W. Nachbauer, and A. J. van den Bogert. Computer simulation of landing movement in downhill skiing: Anterior cruciate ligament injuries. *Journal of Biomechanics*, 29(7):845 – 854, 1996.
- [55] R. McNeill Alexander. Energetics and optimization of human walking and running: the 2000 raymond pearl memorial lecture. *Journal of Human Biology*, 14(5):641–648, 2002.
- [56] M. J. Grey, J. B. Nielsen, N. Mazzaro, and T. Sinkjær. Positive force feedback in human walking. *The Journal of Physiology*, 581(Pt 1):99–105, 2007.
- [57] H. Geyer, A. Seyfarth, and R. Blickhan. Positive force feedback in bouncing gaits? *Proceedings of the Royal Society of London B: Biological Sciences*, 270(1529):2173–2183, 2003.
- [58] A. Wu and Hart. Geyer. The 3-d spring-mass model reveals a time-based deadbeat control for highly robust running and steering in uncertain environments. *IEEE Transactions on Robotics*, 29(5):1114–1124, 2013.
- [59] D. Simon. *Evolutionary Optimization Algorithms: Biologically Inspired and Population-Based Approaches to Computer Intelligence*. John Wiley & Sons Ltd., New York, 2013.
- [60] O. von Stryk and R. Bulirsch. Direct and indirect methods for trajectory optimization. *Annals of Operations Research*, 37(1):357–373, 1992.
- [61] C. Vyasarayani, T. Uchida, J. McPhee, and A. Carvalho. Parameter identification in dynamic systems using the homotopy optimization approach. *Multibody System Dynamics*, 26:411–424, 2011.
- [62] D. Simon. Biogeography-based optimization. *IEEE Transactions on Evolutionary computation*, 12(6):702–713, 2012.
- [63] N. Hansen and A. Ostermeier. Completely derandomized self-adaptation in evolution strategies. *Evolutionary Computation*, 9(2):159–195, 2001.
- [64] H. Herr and J. Markowitz. Human leg model predicts muscle forces, states, and energetics during walking. *PLOS Computational Biology*, 12(5):e1004912, 2016.
- [65] N. Alexander and H. Schwameder. Comparison of estimated and measured muscle activity during inclined walking. *Journal of Applied Biomechanics*, 32(2):150–159, 2016.
- [66] N. Hogan. The mechanics of multi-joint posture and movement control. *Biol. Cybern.*, 52(5):315–331, September 1985.
- [67] E. Vinnars, J. Bergstöm, and P. Fürst. Influence of the postoperative state on the intracellular free amino acids in human muscle tissue. *Annals of Surgery*, 182(6):665–671, 1975.